

# Activation of the ISIS synchrotron room air

B Jones, GJ Burns, HV Cavanagh, DJS Findlay,  
S Karbassi, NA Nilsson, GP Škoro, PNM Wright

November 2021

©2021 UK Research and Innovation



This work is licensed under a [Creative Commons Attribution 4.0 International License](https://creativecommons.org/licenses/by/4.0/).

Enquiries concerning this report should be addressed to:

RAL Library  
STFC Rutherford Appleton Laboratory  
Harwell Oxford  
Didcot  
OX11 0QX

Tel: +44(0)1235 445384  
Fax: +44(0)1235 446677  
email: [libraryral@stfc.ac.uk](mailto:libraryral@stfc.ac.uk)

Science and Technology Facilities Council reports are available online at:  
<https://epubs.stfc.ac.uk>

**DOI: [10.5286/raltr.2021004](https://doi.org/10.5286/raltr.2021004)**

**ISSN 1358-6254**

Neither the Council nor the Laboratory accept any responsibility for loss or damage arising from the use of information contained in any of their reports or in any communication about their tests or investigations.

## Activation of the ISIS synchrotron room air

B Jones<sup>1</sup>, G J Burns, H V Cavanagh, D J S Findlay, S Karbassi, N A Nilsson<sup>2</sup>,  
G P Škoro and P N M Wright

### Abstract

Between February 2018 and February 2020, measurements were made of the activity of the air in the ISIS synchrotron room using a shielded HPGe gamma-ray detector located well outside the synchrotron room, air from the synchrotron room being piped to the detector through a long length of air ducting hose. Overall, more than two thousand separate gamma-ray spectra were recorded. Specific activities were obtained for  $^7\text{Be}$ ,  $^{11}\text{C}$ ,  $^{13}\text{N}$ ,  $^{38}\text{Cl}$ ,  $^{39}\text{Cl}$ ,  $^{40}\text{Cl}$  and  $^{41}\text{Ar}$ , likely radionuclide production routes were identified, and radiation dose rates from submersion in synchrotron room air were obtained. In addition, analyses of many neutron-capture lines were made.

November 2021

---

<sup>1</sup> Present address: European Spallation Source (ESS), Lund, Sweden.

<sup>2</sup> Present address: Center for Quantum Spacetime, Sogang University, Seoul, Korea.

## 1. Introduction

The ISIS Spallation Neutron and Muon Source [1, 2] is driven by an 800-MeV  $\sim 250\text{-}\mu\text{A}$  proton synchrotron running at 50 pulses per second (pps), the synchrotron in turn being driven by a 70-MeV  $\text{H}^-$  drift tube linac. The proton beam from the synchrotron is split and delivered at 40 pps to Target Station 1 (TS-1) and at 10 pps to Target Station 2 (TS-2). Accelerator, proton beam line and target areas are ventilated to avoid build-up of toxic and corrosive gaseous products, to remove heat, to maintain machine areas slightly below atmospheric pressure, and to facilitate the entry of personnel into machine areas after the beam has been switched off.

The ISIS synchrotron is located in an open room 61 metres in diameter and 9 metres in mean height, and this large room acts as a  $\sim 3$ -hour delay/decay tank. Air is drawn into the  $\sim 25000\text{-m}^3$  synchrotron room from ventilated areas around the neutron-producing targets and the proton beam lines through the two  $\sim 100$ -metre-long tunnels for the extracted proton beam lines, and air is extracted from the synchrotron room at a rate of  $2\text{ m}^3\text{ s}^{-1}$  and discharged to atmosphere (authorised by the UK Environment Agency). Schematic diagrams are shown as Figs. 1 and 2.

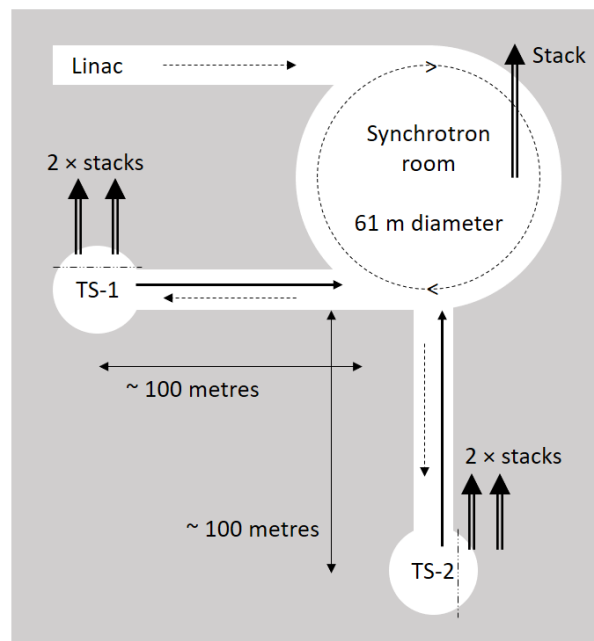


Fig. 1. Schematic diagram of the essential geography of the ISIS Spallation Neutron and Muon Source and its ventilation arrangements. Not to scale!  $\text{H}^-$  beam in the linac and proton beam in the synchrotron delivered to the two target stations shown as dashed arrows. Directions of air flows in tunnels shown as solid arrows. The tunnels between the target stations and the synchrotron have cross-sectional areas of  $\sim 7\text{--}8\text{ m}^2$ . The 52-metre-diameter ISIS synchrotron is located in the open 61-metre-diameter  $\sim 8\text{--}9$ -metre high synchrotron room. The discharge stack from the synchrotron room, which is the same as the  $2\text{ m}^3\text{ s}^{-1}$  stack shown in Fig. 2, is actually located in Building R4 which contains the air-conditioning plant for the synchrotron room. The discharge stacks for TS-2 are shown offset for clarity.

At the heart of each of the two target stations TS-1 and TS-2 is a neutron-producing target (together with moderators and a reflector) surrounded by a monolith which consists of several thousand tons of steel and concrete shielding. In order to be able to switch on and off beams of neutrons to the research instruments in the experimental

halls independently, massive ~20-ton movable steel shutters are incorporated in the monoliths, and these shutters move in voids within the steel in the monolith. The shutter voids are ventilated, and the air from the shutter voids is drawn into the synchrotron room through the proton beam line tunnels shown in Figs. 1 and 2.

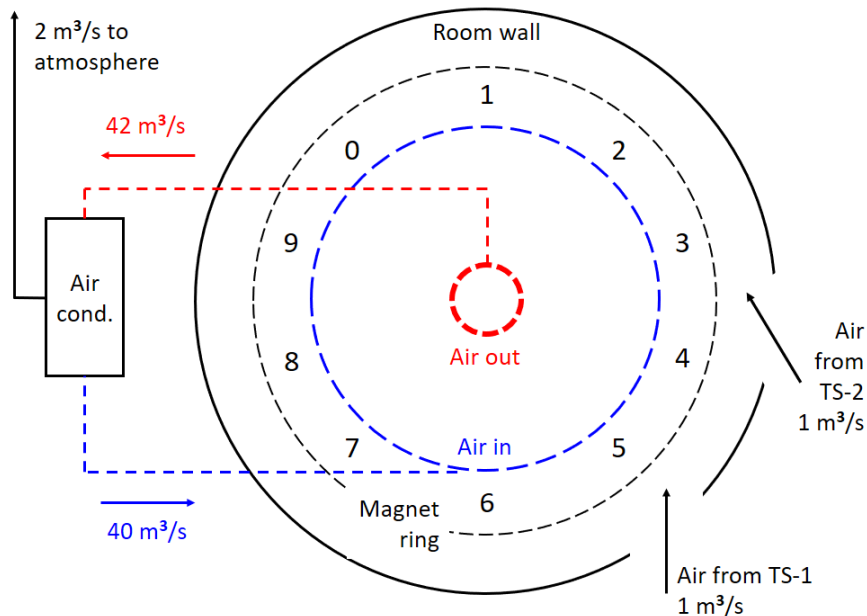


Fig. 2. Schematic diagram of air flows into and out of the ISIS synchrotron room. Air from the full-flow-filtered air-conditioning system enters at floor level, and leaves at ceiling level. The numbers 0–9 denote the positions of the ten superperiods (SPs) of the synchrotron (injection takes place in SP0, and collimation and extraction take place in SP1). The air from Target Stations TS-1 and TS-2 is essentially ventilation air from the shutter voids in the several-thousands-of-tons monoliths of steel and concrete shielding around the neutron-producing targets. Air is discharged to atmosphere at a nominal rate of  $2 \text{ m}^3 \text{ s}^{-1}$  through a stack on the roof of the air-conditioning building.

## 2. Measurements

Because the synchrotron structure and its surroundings inevitably become slightly radioactive in use, it is not practical to make measurements of activated air within the synchrotron room simply by using a health physics monitor, since background from activated machine components and support structures is always present. Consequently, a method was developed whereby air from the synchrotron room is sucked out along a 76-metre length of 10-cm-diameter flexible PVC air ducting hose, a fraction of this air is then circulated through a thin-walled aluminium cylindrical vessel with an internal volume and diameter of  $859 \text{ cm}^3$  and 9.3 cm respectively immediately in front of a shielded Canberra BE3825 HPGe gamma-ray detector, and the air is then returned to the synchrotron room. The time for activated air to travel from the input end of the long flexible tube to the HPGe was measured using a smoke generator and found to be  $69 \pm 5$  seconds [3]. The HPGe detector was located in the corridor of Building R52 as shown in Fig. 3, and a schematic diagram of the air-flow path to and from the detector is shown as Fig. 4. Ten sets of gamma-ray spectra spanning a period of time of two years were recorded as listed in Table 1. Overall, 2363 separate gamma-ray spectra were accumulated.

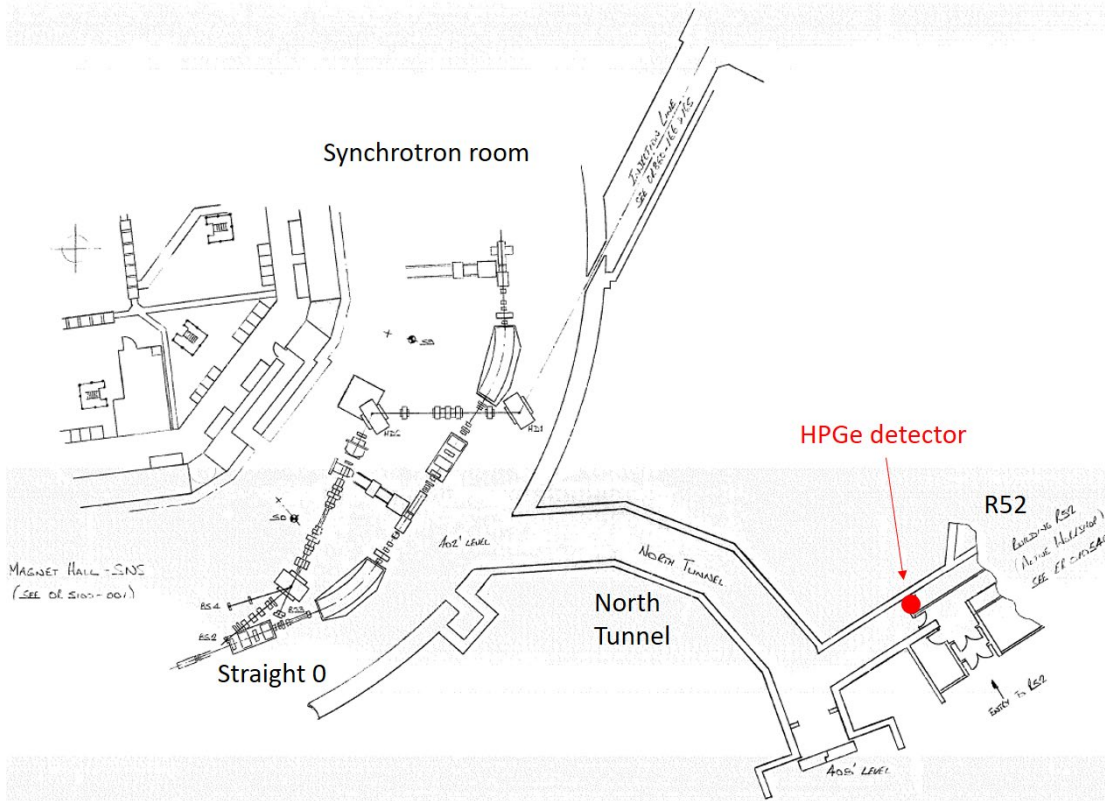


Fig. 3. Location of HPGe gamma-ray detector in the corridor of Building R52 adjoining the North Tunnel leading from the 200-foot-diameter ISIS synchrotron room to Road 1. From drawing 0-SI-5100-088\_00\_A. There is a height difference of 6 feet between the beginning (402 feet above sea level) and the end (408 feet above sea level) of the North Tunnel.

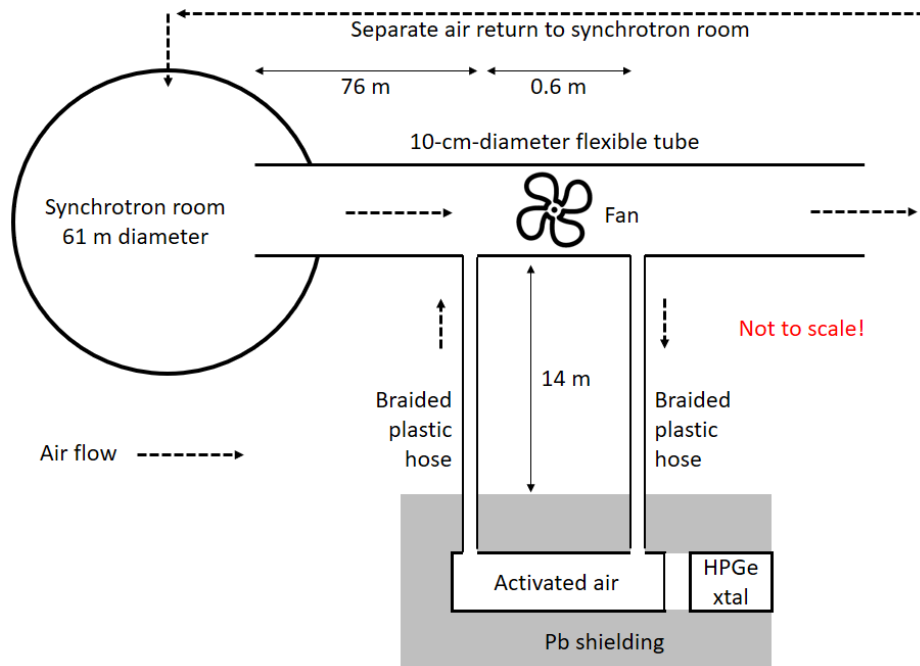


Fig. 4. Schematic representation of air from the ISIS synchrotron room being passed continuously in front of the BE3825 Canberra HPGe gamma-ray detector located in R52. Not to scale! The volume of the activated air sample vessel in front of the HPGe detector is 859 cm<sup>3</sup>.

Dates	No. of spectra	Tot. real time, s	Tot. live time, s	Air sampled from
27 Feb. – 02 Mar 2018	245	220500	220039	Foil change area
23 – 26 Mar. 2018	254	228600	228222	SP0 and 9 datum points
01 – 03 May 2018	194	174600	174261	SP9 datum point and SP6 bridge
12 – 14 Jul. 2018	355	319500	318903	Hall 2 bridge (inner)
25 – 28 Oct. 2018	282	253800	253282	Hall 2 bridge (inner)
18 – 20 Dec. 2018	197	177300	176961	Hall 2 bridge (inner)
27 Mar. – 02 Apr. 2019	515	463500	462607	Hall 2 bridge (inner)
22 Oct. 2019	6	5400	5390	Hall 2 bridge (inner)
19 – 23 Dec. 2019	181	325800	325250	Hall 2 bridge (inner)
25 – 28 Feb. 2020	129	231300	230920	Hall 2 bridge (inner)

Table 1. Summary of ten sets of gamma-ray spectra from activated synchrotron room air. All individual gamma-ray spectra ran for a real time of 900 seconds, except for the December 2019 and February 2020 spectra which all ran for a real time of 1800 seconds. Counting rate losses were minimal; dead times all lay within the range 0.16–0.21%. The sum of real and live times for all ten sets of spectra is 28 days.

Successive 15-minute-long gamma-ray spectra<sup>3</sup> were recorded and stored over periods of two or three days — each usually covering a period of 2–3 days beginning just before the end of an irradiation campaign (‘user cycle’) and ending after a further ~1–2 days of accelerator physics work. A typical 15-minute-long gamma-ray spectrum when the synchrotron was running steadily is shown in Fig. 5, in which the only prominent gamma-ray lines are at 511 keV (from positron emitters such as <sup>11</sup>C, <sup>13</sup>N and <sup>15</sup>O) and at 1294 keV (from <sup>41</sup>Ar from neutron capture on the ~1% of argon naturally present in air). The beginnings and ends of counting periods were taken from the corresponding times recorded within the spectrum files themselves (correcting for two changes of local time from GMT (Greenwich Mean Time) to BST (British Summer Time)). Fig. 6 shows a representative set of data collected: counts per 15 minutes in 511- and 1294-keV peaks, and beam current from the synchrotron measured at 4-minute intervals.

<sup>3</sup> As stated in the caption to Table 1, the spectra for the December 2019 and February 2020 sets of data were each 30 minutes long, not 15 minutes long.

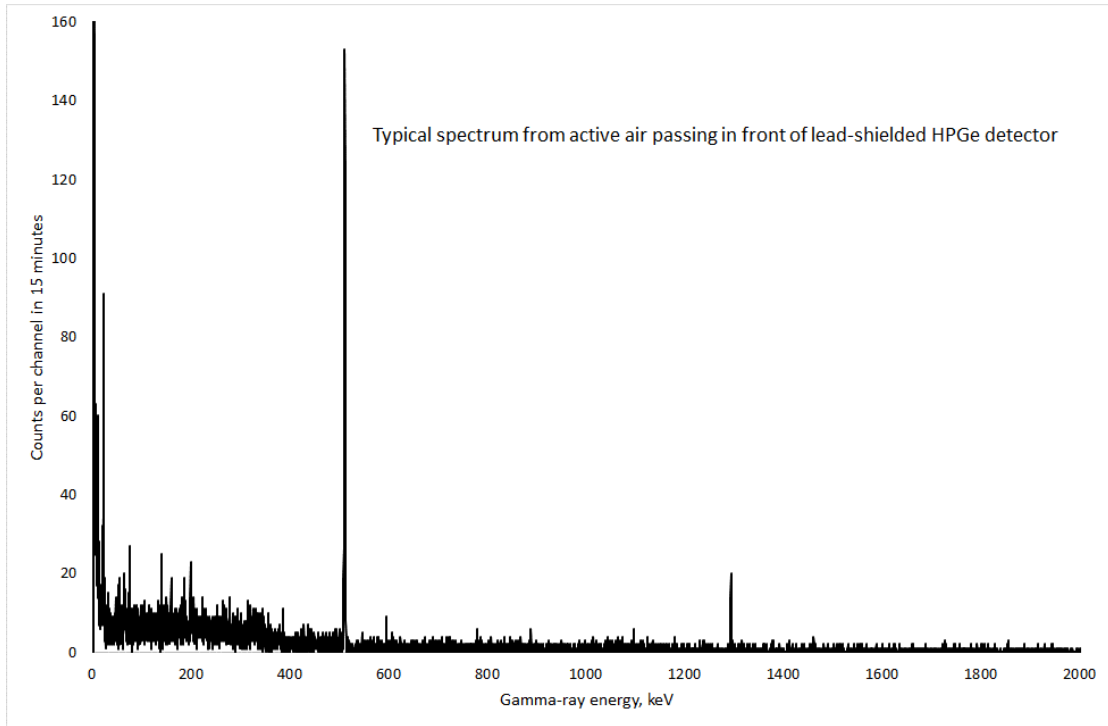


Fig. 5. Typical gamma-ray energy spectrum seen by the HPGe detector. The lines at 511 keV from positron-emitting radionuclides such as  $^{11}\text{C}$ ,  $^{13}\text{N}$  and  $^{15}\text{O}$ , and at 1294 keV from  $^{41}\text{Ar}$ , stand out very clearly.

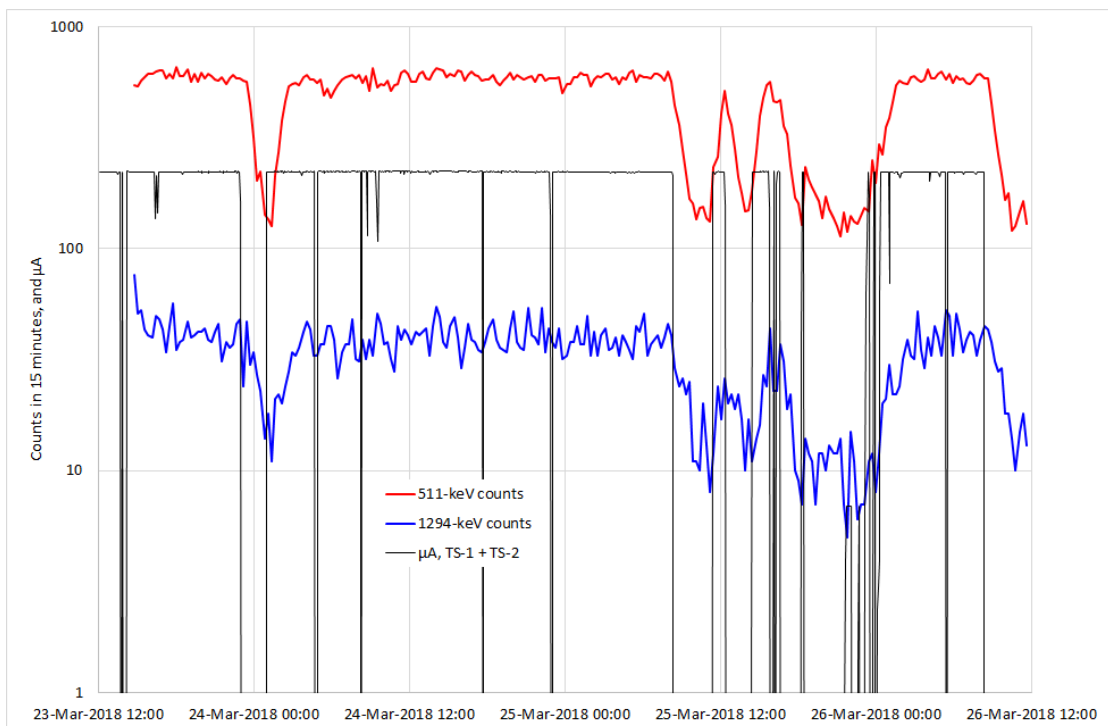


Fig. 6. Representative data set covering three days: counts in 15 minutes in 511- and 1294-keV peaks in gamma-ray spectra, and the synchrotron proton beam current (which is the sum of beam currents delivered to target stations TS-1 and TS-2).

### 3. Major radionuclides

In this section are discussed the ‘major’ radionuclides in the air of the ISIS synchrotron room, *viz* the positron-emitting radionuclides  $^{11}\text{C}$ ,  $^{13}\text{N}$  and  $^{15}\text{O}$  (from knock-out reactions and spallation in the nitrogen and oxygen in the air), and  $^{41}\text{Ar}$  (from neutron capture on the  $\sim 1\%$  of argon naturally present in air). The three radionuclides  $^{11}\text{C}$ ,  $^{13}\text{N}$  and  $^{15}\text{O}$  emit no gamma-rays directly, so separation of the contributions that  $^{11}\text{C}$ ,  $^{13}\text{N}$  and  $^{15}\text{O}$  make to 511-keV annihilation gamma-rays has to be made on the basis of half-lives.

#### 3.1 Model

In order to extract information from sets of data such as the set illustrated in Fig. 6, the following model was adopted. Wherever in the ISIS facility they were produced, radionuclides in air were assumed to be produced at rates proportional to the proton beam current. Allowance was made for an interval of time to elapse between production of this air activity and the appearance of the activity in the synchrotron room. Once in the synchrotron room, some of the activity was assumed to decay in the normal way, and some of the activity was assumed to be removed via the discharge stack shown in Fig. 1. Allowance was also made for the interval of time it took for air to travel from the synchrotron room to the HPGe gamma-ray detector. Appendix 1 gives an expression for the number of counts  $c_{i,j}$  in the HPGe detector from radionuclide  $i$  over a counting interval  $\Delta$  beginning at time  $t_j$ , and also describes how this expression is fitted to the data.

#### 3.2 Half-life of 511-keV component

It is clear that the half-life of the 1294-keV component should correspond to the 110-minute half-life of  $^{41}\text{Ar}$ , but the 511-keV component could be due to some or all of  $^{11}\text{C}$ ,  $^{13}\text{N}$  and  $^{15}\text{O}$  with half-lives of 20.3, 9.96 and 2.03 minutes respectively, since these three radionuclides can all be produced by nuclear reactions in the air and they emit only positrons when they decay. Fig. 7 shows the 511-keV component for a typical beam-on-to-beam-off transition. Also shown is the rate at which  $^{11}\text{C}$  alone would decay, taking into account the air extraction rate from the synchrotron room, *i.e.* the dashed line is proportional to  $\exp(-\lambda'(t - t_0))$  where  $\lambda' = \lambda_{11\text{C}} + v/V$  is the effective  $^{11}\text{C}$  decay constant,  $\lambda_{11\text{C}} = \ln(2)/t_{1/2,11\text{C}}$  where  $t_{1/2,11\text{C}} = 20.3$  minutes,  $v$  and  $V$  are the air exchange rate and synchrotron room volume respectively and have values of  $2 \text{ m s}^{-1}$  and  $25000 \text{ m}^3$  respectively, and  $t_0$  is the beam-off time. Since the effective half-life  $t'_{1/2} = \ln(2)/\lambda' = 17.8$  minutes, it seems clear that the measured data support the conclusion that the 511-keV activity is mostly due to  $^{11}\text{C}$  alone.

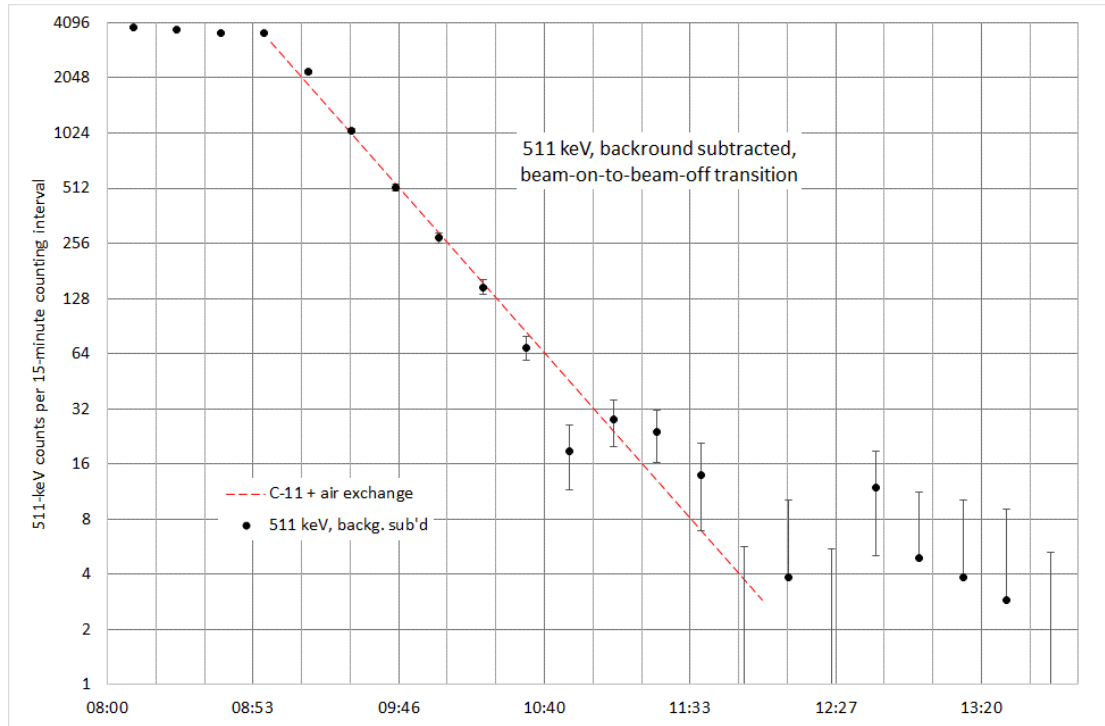


Fig. 7. 511-keV component of counts in HPGe detector after background subtraction for a typical beam-on-to-beam-off transition, plotted on a base-2 logarithmic scale with 17.8-minute intervals (the effective  $^{11}\text{C}$  half-life taking into account air exchange in the synchrotron room) marked on the horizontal axis. The dashed line is a decay proportional to  $2^{-t/(17.8 \text{ minutes})}$ . It is evident that the decay corresponds almost entirely to the decay of  $^{11}\text{C}$ .

It will be shown in Sect. 3.3 below that a time interval of  $\sim 10$  minutes elapses between creation of activity in the air and measurement of the air activity in the synchrotron room. Since the half-life of  $^{15}\text{O}$  is  $\sim 2$  minutes, it is not surprising that Fig. 7 shows little or no evidence for the present of  $^{15}\text{O}$ , since some five half-lives will have elapsed between creation of  $^{15}\text{O}$  activity and measurement of  $^{15}\text{O}$  activity. However, it is surprising that not more  $^{13}\text{N}$  is apparently present in Fig. 7, since the half-life of  $^{13}\text{N}$  is  $\sim 10$  minutes, and so only one half-life will have elapsed. In the neutron-dominated radiation fields prevailing in the accelerator, target and beam-line areas, the most likely production routes for  $^{13}\text{N}$  and  $^{15}\text{O}$  from the nitrogen and oxygen in the air could be expected to be the  $^{14}\text{N}(n,2n)^{13}\text{N}$  and  $^{16}\text{O}(n,2n)^{15}\text{O}$  reaction channels respectively, whereas the most likely production route for  $^{11}\text{C}$  from the nitrogen and oxygen in the air could be expected to be the  $^{14}\text{N}(n,nt)^{11}\text{C}$  and  $^{16}\text{O}(n,2n\alpha)^{11}\text{C}$  reaction channels. Above a few MeV, the energy spectrum of proton-produced neutrons has a tail that decreases monotonically as the neutron energy increases [4], and since the threshold energies of the  $^{14}\text{N}(n,2n)$ ,  $^{16}\text{O}(n,2n)$ ,  $^{14}\text{N}(n,nt)$  and  $^{16}\text{O}(n,2n\alpha)$  reactions are 11.3, 16.7, 24.4 and 27.5 MeV respectively [5], significantly more  $^{13}\text{N}$  would be expected to be produced than  $^{11}\text{C}$ , as anticipated in the results of exploratory MCNPX and CINDER-90 Monte Carlo calculations [6] carried out at ISIS which suggested that  $^{13}\text{N}$  should account for  $\sim 70\%$  of the activity of the air in the synchrotron room at saturation. How can the differences amongst these expectations, calculated results and the results of the present measurement be best explained? Consideration of this question is deferred until Sect. 3.5 below.

### 3.3 Delay times

With the assumption that that the 511-keV component seen by the HPGe detector is due to  $^{11}\text{C}$  alone (so that in Appendix 1  $m = 2$ ), eight data sets (the one shown in Fig. 6 and seven others) were fitted using the model outlined in Sect. 3.1. A typical fit is shown in Fig. 8, and results are set out in Table 2. However, in view of the possibility that the 511-keV component does in fact contain a significant contribution from  $^{13}\text{N}$ , Table 2 also lists results assuming that the 511-keV component seen by the HPGe detector is due to  $^{13}\text{N}$  alone. Whilst some of the fits in Table 2 are undoubtedly poor, the explanation being that the fits include periods of time when the synchrotron was not running normally but was being used for accelerator physics purposes when beam delivery and beam conditions are often well outside normal operational envelopes, it is evident that the fits are on average better assuming that the 511-keV component is due to  $^{11}\text{C}$  alone than assuming it to be due to  $^{13}\text{N}$  alone, and that the overall time from source to detector ranges between roughly 12 and 20 minutes depending on location within the synchrotron room.

With what can these times be compared? At ISIS the most likely places for air to be activated are the shutter voids in the massive shielding monoliths surrounding the neutron-producing targets (see Sect. 1) where high fluxes of neutrons pass through the ventilating air. Elsewhere, little activity in air is likely to be produced, as beam losses around the synchrotron and along the proton beam transport lines are low [7] — confirmation being that when beam losses around the synchrotron were deliberately doubled no increase in activation was observed. Using a smoke generator, the mean time for air to be moved by the ventilation systems from the shutter voids to the synchrotron room was measured [8] as 8 minutes, with a spread of  $\pm 4$  minutes. This mean time of 8 minutes, with two additions, *viz* the few minutes for air to be moved by the air-conditioning system circulating air through the synchrotron room from the point where the air from the shutter voids enters the synchrotron room to the point where the air is sampled, and the  $\sim 1$  minute for air to travel from the sampling point to the HPGe gamma-ray detector, is in satisfactory agreement with the  $\sim 12$ – $20$  minutes obtained from the fits.

Date of measurement	Location from which air being sampled is drawn	511 keV = $^{11}\text{C}$		511 keV = $^{13}\text{N}$	
		$\delta_s + \delta_c$ , minutes	$\chi_{\text{pdf}}^2$	$\delta_s + \delta_c$ , minutes	$\chi_{\text{pdf}}^2$
Feb. 2018	Foil change area, SP0	$15.1 \pm 0.3$	3.99	$22.6 \pm 8.01$	6.48
Mar. 2018	SP0/9 datum points	$18.2 \pm 2.1$	2.05	$26.6 \pm 12.4$	3.46
May 2018	SP9 datum and SP6 bridge	$16.8 \pm 1.0$	7.49	$23.6 \pm 1.5$	11.4
Jul. 2018	Inner side of SP5/6	$15.0 \pm 0.6$	19.2	$15.2 \pm 0.5$	21.2
Oct. 2018	Inner side of SP5/6	$14.0 \pm 0.5$	31.5	$14.0 \pm 0.9$	21.8
Dec. 2018	Inner side of SP5/6	$14.2 \pm 0.4$	20.1	$14.8 \pm 0.4$	30.6
Apr. 2019	Inner side of SP5/6	$15.0 \pm 1.4$	23.7	$17.1 \pm 2.3$	34.2
Dec. 2019	Inner side of SP5/6	$12.5 \pm 0.7$	87.3	$14.8 \pm 8.6$	93.6
Feb. 2020		[Data timings unavailable]			

Table 2. Sums of source-to-synchrotron-room and synchrotron-room-to-HPGe delay times from fitting eight sets of data (the individual delay times  $\delta_s$  and  $\delta_c$  are essentially completely anti-correlated) for two ‘extreme’ assumptions, *viz* assuming that the 511-keV activity is due entirely to  $^{11}\text{C}$ , and assuming that the 511-keV activity is due entirely to  $^{13}\text{N}$ . The fits include incorporation of a rectangular distribution  $s$  as described in Sect. 3.1 spanning a range of  $\pm 4$  minutes representing the spread in the nominal time  $\delta_s$  for activated air to travel from the production source to the synchrotron room. The uncertainties quoted were obtained by perturbing one hundred times the counts  $C_{i,j}$  per 15-minute (or 30-minute) counting period by amounts chosen from random gaussian distributions with standard deviations  $\delta C_{i,j}$  and then taking the standard deviations of the one hundred perturbed values of  $\delta_s + \delta_c$ , and finally, in accordance with ‘external consistency’, multiplying by  $\chi_{\text{pdf}}^2$ <sup>1/2</sup>.

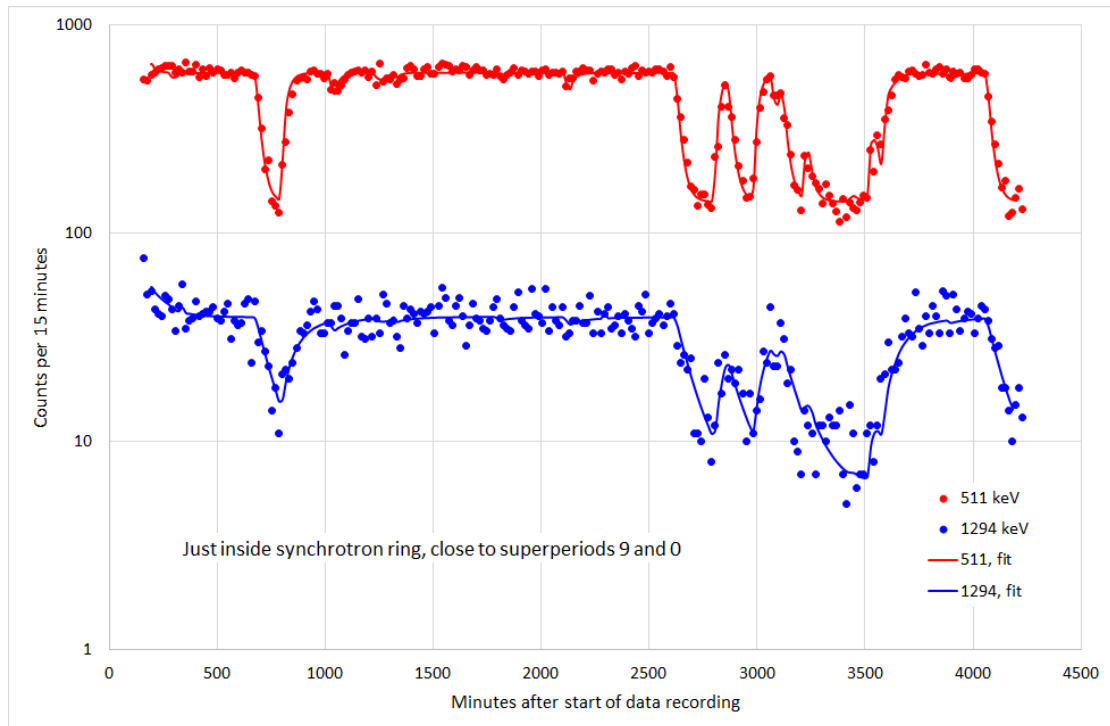


Fig. 8. Fits to 511- and 1294-keV data measured during 23–26 March 2018. The fits are as described in Sect. 3.1.

### 3.4 Specific activity of air

For both 511- and 1294-keV activity, the specific activity  $a$  of the air ( $\text{Bq cm}^{-3}$ ) sampled from the synchrotron room was calculated from  $a = 2^{(\delta_c/t_{1/2})} \dot{C} / (\alpha \varepsilon V_{\text{vessel}})$  where  $\delta_c$  is the synchrotron-room-to-HPGe-detector delay time,  $t_{1/2}$  is the half-life of the corresponding radionuclide,  $\dot{C}$  is the count rate of the 511- or 1294-keV component of the gamma-ray spectrum when the synchrotron is running steadily (e.g. the count rate corresponding to the ‘high flat’ parts of the 15-minute-counts data shown in Fig. 6),  $\alpha$  is the emission probability (‘abundance’) of the gamma-rays being counted, and  $\varepsilon$  is the full-energy-peak efficiency for counting gamma-rays from the activated air vessel of volume  $V_{\text{vessel}}$  just in front of the HPGe detector. The full-energy-peak efficiency for the HPGe detector at 511 keV was calculated as  $\varepsilon_{511} = 0.0122 \pm 0.0024$  by integrating the point-source full-energy-peak efficiency of the detector over the surface area of the inside of the activated air vessel using MORSE [9] with the DLC37F library [10], and the full-energy-peak efficiency at 1294 keV was integrated in a similar way over the volume of the vessel to give  $\varepsilon_{1294} = 0.00388 \pm 0.00078$  (the range in air of the 385-keV-mean-energy positrons from  $^{11}\text{C}$ ,  $\sim 100$  cm, is much greater than the characteristic dimension of the vessel, and so most positrons annihilate on the inner surface of the vessel). In view of the conclusion of Sect. 3.2 and anticipating the conclusion of Sect. 3.5 that the 511-keV component is largely due to  $^{11}\text{C}$ , from the half-lives of  $^{11}\text{C}$  and  $^{41}\text{Ar}$  of 20.3 and 110 minutes respectively, and from the gamma-ray emission probabilities per becquerel for  $^{11}\text{C}$  and  $^{41}\text{Ar}$  of 1.9952 and 0.9916 respectively, results for the specific activity  $a$  are presented in Table 3. Representative values for the specific activities of  $^{11}\text{C}$  and  $^{41}\text{Ar}$  in the air in the synchrotron room are  $\sim 0.10$  and  $\sim 0.03$   $\text{Bq cm}^{-3}$  respectively.

### 3.5 Search for $^{13}\text{N}$ component of 511-keV activity

The extent to which the 511-keV activity is due to  $^{11}\text{C}$  was investigated by simultaneously fitting the 511- and 1294-keV counts  $C_{511,i}$  and  $C_{1294,i}$  in the 15-minute bins  $i$  during beam-on-to-beam-off transitions with the expressions  $C'_{511,i} = C'_{^{13}\text{N},i} + C'_{^{11}\text{C},i} + b_{511}(t_i - t_{i-1})$  and  $C'_{1294,i} = C'_{^{41}\text{Ar},i} + b_{1294}(t_i - t_{i-1})$  where the  $C'_{AZ,i}$ 's are the expressions  $C'(t_1, t_2) = \int_{t_1}^{t_2} c'(t) dt$  given in Appendix 2 with  $t_1 = t_{i-1}$ ,  $t_2 = t_i$ ,  $\lambda = \lambda_{AZ} + r_{\text{exch}}/V$  where  $\lambda_{AZ} = \ln(2)/t_{1/2,ZA}$  and  $t_{1/2,ZA}$  is 9.96, 20.3 and 110 minutes for  $^{13}\text{N}$ ,  $^{11}\text{C}$  and  $^{41}\text{Ar}$  respectively, and  $w = 4$  minutes. The expressions for  $C'(t_1, t_2)$  were used because during the measurement of the time for air to be moved by the ventilation systems from the shutter voids to the synchrotron room (see Sect. 3.3) it was observed that by the time a short burst of smoke in the shutter void had reached the synchrotron room it had spread out in time over  $\pm 4$  minutes. The seven fitted parameters are  $c_{0,^{13}\text{N}}$ ,  $c_{0,^{11}\text{C}}$ ,  $c_{0,^{41}\text{Ar}}$ ,  $b_{511}$ ,  $b_{1294}$ ,  $r_{\text{exch}}$  and  $t_{\text{off}}$  where  $c_{0,^{13}\text{N}}$ ,  $c_{0,^{11}\text{C}}$  and  $c_{0,^{41}\text{Ar}}$  are the steady-state count rates  $c_0$  in the expressions in the Appendix for  $^{13}\text{N}$ ,  $^{11}\text{C}$  and  $^{41}\text{Ar}$  respectively,  $b_{511}$  and  $b_{1294}$  are the corresponding background rates for the 511- and 1294-keV signals,  $r_{\text{exch}}$  is the air exchange rate at the position where the measurements are being made, and  $t_{\text{off}}$  is the beam-off time (since beam-off times are not synchronised with the ‘15-minute clock’ of the gamma-ray counting régime). Results are given in Table 4, and one of the fits is shown in Fig. 9. From Table 4, it is clear that the 511-keV activity is nearly all due to  $^{11}\text{C}$ , in agreement with the earlier conclusion in Sect. 3.2 — and, incidentally, in accordance with the suggestion [11] that on balance most of the 511-keV air activity is more likely to be due to  $^{11}\text{C}$  than to  $^{13}\text{N}$ .

Date of measurement	Location	Counts / 15 minutes, 511 keV	Counts / 15 minutes, 1294 keV	Bq cm <sup>-3</sup> , <sup>11</sup> C	Bq cm <sup>-3</sup> , <sup>41</sup> Ar	Bq cm <sup>-3</sup> , <sup>11</sup> C ÷ Bq cm <sup>-3</sup> , <sup>41</sup> Ar
Feb. 2018	Foil change area, SP0	1500 ± 50	100 ± 5	0.083 ± 0.017	0.034 ± 0.007	2.5 ± 0.1
Mar. 2018	SP0/9 datum points	550 ± 25	40 ± 5	0.030 ± 0.006	0.014 ± 0.003	2.2 ± 0.3
May 2018	SP9 datum point and SP6 bridge	1550 ± 50	105 ± 10	0.086 ± 0.018	0.036 ± 0.008	2.4 ± 0.2
Jul. 2018	Inner side of SP5/6	4200 ± 200	155 ± 15	0.233 ± 0.049	0.053 ± 0.012	4.4 ± 0.5
Oct. 2018	Inner side of SP5/6	2900 ± 150	100 ± 10	0.161 ± 0.034	0.034 ± 0.008	4.7 ± 0.5
Dec. 2018	Inner side of SP5/6	3700 ± 150	140 ± 15	0.205 ± 0.043	0.047 ± 0.011	4.3 ± 0.5
Apr. 2019	Inner side of SP5/6	4000 ± 200	150 ± 15	0.222 ± 0.047	0.051 ± 0.012	4.4 ± 0.5
Dec. 2019	Inner side of SP5/6	4550 ± 200	155 ± 10	0.252 ± 0.053	0.053 ± 0.011	4.8 ± 0.4
Feb. 2020	Inner side of SP5/6	2000 ± 100	100 ± 10	0.111 ± 0.024	0.034 ± 0.008	3.3 ± 0.4
Means and standard deviations				0.099 ± 0.070	0.032 ± 0.013	0.131 ± 0.071

Table 3. Specific activity of air samples from the synchrotron room when the synchrotron was running steadily. Although there are nine sets of data, there are data sets for only four distinct locations, and so the six measurements made in the same place have themselves been averaged before the means and standard deviations are taken. In the rightmost column the uncertainties are the statistical uncertainties from the counts in the peaks in the gamma-ray spectrum only, as the detection efficiency of the HPGe gamma-ray detector is a common factor in the <sup>11</sup>C and <sup>41</sup>Ar specific activities. Whilst in the February 2020 data set the timing data were unavailable, as indicated in Table 2, count rates with the beam on and off were still perfectly visible.

Location	Date	$c_{0,13N}$ min <sup>-1</sup>	$c_{0,11C}$ min <sup>-1</sup>	$c_{0,41Ar}$ min <sup>-1</sup>	$b_{511}$ min <sup>-1</sup>	$b_{1294}$ min <sup>-1</sup>	$r_{\text{exch}}$ m <sup>3</sup> s <sup>-1</sup>	$t_{\text{off}}$ mins.	$\chi_{\text{pdf}}^2$
SP0	Feb. 2018	$-67 \pm 17$	$163 \pm 17$	$6.4 \pm 0.1$	$2.8 \pm 0.1$	$0.08 \pm 0.01$	$3.8 \pm 0.3$	$\pm 2.0$	1.20
SP0 (no -ve's)		$0 \pm 0.01$	$96.0 \pm 0.4$	$6.4 \pm 0.1$	$2.9 \pm 0.1$	$0.08 \pm 0.01$	$3.7 \pm 0.4$	$\pm 1.0$	1.33
SP9, 6	May 2018	$-89 \pm 27$	$183 \pm 27$	$6.9 \pm 0.1$	$2.4 \pm 0.1$	$0.08 \pm 0.03$	$3.5 \pm 0.5$	$\pm 3.8$	1.93
SP9, 6 (no -ve's)		$0 \pm 0.07$	$93.1 \pm 0.5$	$6.7 \pm 0.2$	$2.4 \pm 0.1$	$0.07 \pm 0.03$	$3.5 \pm 0.5$	$\pm 1.5$	2.12
SP5,6	Dec. 2018	$6 \pm 21$	$223 \pm 21$	$8.6 \pm 0.1$	$2.2 \pm 0.1$	$0.09 \pm 0.03$	$4.1 \pm 0.4$	$\pm 0.9$	1.91

Table 4. Results of seven-parameter fits to beam-on-to-beam-off transitions, with inclusion of rectangular time-dispersion function of half-width 4 minutes as described in the text. The uncertainties have been obtained by the same method as that described in the caption to Table 2. The values of the chi-squared of the fit per degree of freedom  $\chi_{\text{pdf}}^2$  are also shown. Results of two fits for locations SP0 and SP9+6 are shown; in the second of each pair of fits all parameters were forced to be non-negative during the fitting process. The absolute value of  $t_{\text{off}}$  is irrelevant, as all that matters is the uncertainty with which it can be defined. In the rows for SP0 and SP9+6 where negative values are allowed, the parameters  $c_{13N}$  and  $c_{11C}$  are, not surprisingly, very highly anti-correlated. (The February, May and December 2018 data sets are the only data sets for which the timing bins are 15 minutes wide and in which there is at least twelve hours of steady running before beam-off and twelve hours after beam-off to establish background.) The fitted value of  $r_{\text{exch}}$ , the rate of air exchange in the synchrotron room, is a little greater than the nominal air extraction rate of  $2 \text{ m}^3 \text{ s}^{-1}$ , but this may be a consequence of likely non-uniform patterns of air movements within the synchrotron room.

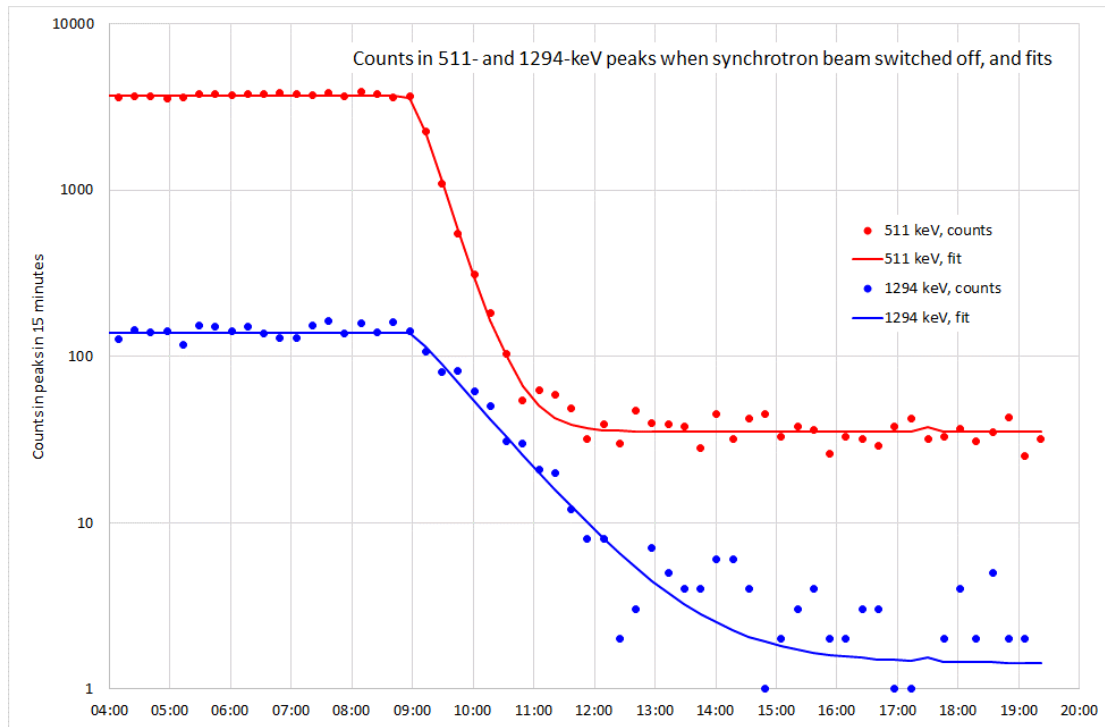


Fig. 9. Typical 7-parameter simultaneous fits to 511- and 1294-keV lines when synchrotron beam is switched off. This fit is for the December 2018 data, where the activated air was sampled close to the inner side of the synchrotron ring between superperiods 5 and 6.

### 3.6 Comparison with results from discharge stack monitor

Air from the ISIS synchrotron room is exhausted to atmosphere through a filtered stack (the stack is included schematically in Figs. 1 and 2), and a drum-and-Geiger-tubes system [11] is used to monitor the activity in the air being discharged. The sensitivities of the monitoring system are respectively  $5330 \pm 690$  and  $3730 \pm 340$  Bq m<sup>-3</sup> cps<sup>-1</sup> for <sup>11</sup>C and <sup>41</sup>Ar in air, decay-curve measurements show [11] that essentially two-thirds of the activity is due to <sup>11</sup>C and one-third to <sup>41</sup>Ar, and the system typically counts at rates in the range of 25–30 cps. Consequently, including decay of <sup>11</sup>C and <sup>41</sup>Ar over the 10 minutes it takes on average for air to be circulated once through the synchrotron room [11], the specific activity of the air in the synchrotron room deduced from the stack monitor is  $0.174 \pm 0.026$  Bq cm<sup>-3</sup> — a value consistent with the results from the HPGe detector in the present work.

### 3.7 Discussion

Why, contrary to the expectations referred to in Sect. 3.2 that <sup>13</sup>N should make the largest contribution to 511-keV activity, might the 511-keV activity in the air in the synchrotron room be largely due to <sup>11</sup>C? A first possible explanation could simply be that the Monte Carlo calculations referred to in Sect. 3.2 did not include all routes for the production of activity. The calculations included incident neutron energies up to 25 MeV, which ought to be sufficiently high to include most of the <sup>14</sup>N(n,2n) cross-section [12] for the most plentiful component (nitrogen) of air especially in view of the  $\sim E^{-3/2}$  energy dependence [4] of the spallation neutron spectrum, but it may be that higher-energy neutrons that induce spallation reactions in the air play a part. Neglecting

the difference between neutron-induced and proton-induced spallation, the cross-sections for the production of  $^{11}\text{C}$  and  $^{13}\text{N}$  from nitrogen and oxygen by spallation lie in the ranges  $\sim 10\text{--}20$  and  $\sim 5\text{--}10$  millibarns respectively [13]. In order to produce a saturation activity of  $\sim 0.10\text{--}0.15\text{ Bq cm}^{-3}$  (see Table 3) in the air in the synchrotron room by spallation, the effective flux of neutrons inducing spallation in the TS-1 shutter void would have to be  $\sim 4\text{--}5 \times 10^5\text{ cm}^{-2}\text{ s}^{-1}$ , and such a flux is not entirely inconsistent with the geometry and materials in the TS-1 monolith and the TS-1 neutron source term of  $2 \times 10^{16}\text{ s}^{-1}$  [14].

A second possible explanation could be that some chemical or filtering process preferentially removes  $^{13}\text{N}$  from the air (air from the shutter voids does pass through HEPA filters). It could be that the nitrogen activity is accompanied by radiolytic production of  $\text{NO}_x$  (nitrogen oxide), some of the  $\text{NO}_x$  being then effectively removed chemically through combination with water vapour [15]. Such a possibility is not inconsistent with corrosion of metal surfaces observed in practice in and around the TS-1 target monolith.

A third possible explanation could be that after its production the activated air takes so long to reach the HPGe detector that the  $^{13}\text{N}$  has mostly decayed. It was seen in Sect. 3.3 that the delay time between production of activity and detection of activity in the HPGe gamma-ray detector is  $\sim 12\text{--}20$  minutes, and this is consistent with the delay time of  $22 \pm 2$  minutes [11] observed between production of activity and detection of activity in the permanently installed drum-and-Geiger-tubes system monitoring the activity of air discharged from the synchrotron room, since it takes several minutes for air from the synchrotron to reach the drum-and-Geiger-tubes monitoring system whereas it takes only  $\sim 1$  minute for air from the synchrotron to reach the HPGe detector. But even if the upper end of the  $\sim 12\text{--}20$ -minutes range were assumed, and even if an extra  $\sim 10$  minutes were added to account for incomplete mixing of air in the synchrotron room until the air has passed once around the synchrotron room air circulation system (synchrotron room volume  $\sim 25000\text{ m}^3$ , air circulation speed  $\sim 40\text{ m}^3\text{ s}^{-1}$ ), the resultant  $\sim 30$  minutes would reduce  $^{13}\text{N}$  activity relative to  $^{11}\text{C}$  activity by a factor of only  $\sim 2.8$ , and the application of such a factor to the results of the Monte Carlo calculations referred to in Sect. 3.2 would be insufficient to reproduce the apparent paucity of  $^{13}\text{N}$  in the measured data.

All things considered, the most plausible explanation may be that spallation plays an important part in activation of the air and that the chemical removal of  $^{13}\text{N}$  is not negligible. It may be noted that in the NuMI facility at Fermilab [16] and in spallation at KEK [17] the measured values of  $^{11}\text{C}$  and  $^{13}\text{N}$  specific activity in activated air are in the ratios of  $1.6 : 1.0$  and  $2.3 : 1.0$  respectively. It would be worthwhile to perform Monte Carlo calculations with highly detailed models of the entire ISIS TS-1 and TS-2 monoliths (including detailed models of the shutters and detailed models of the target, reflector and moderators (TRAM) assemblies) and tracking all particles with energies up to 800 MeV, but the effort to perform such calculations would not be trivial.

It is noticeable in Table 2 that overall source-to-detection times  $\delta_s + \delta_c$  are one or two minutes greater for air sampled from near superperiods (SPs) 0 and 9 than for air sampled from near SPs 5 and 6. This is not inconsistent with the facts that these two air-sampling positions (near SPs 0 and 9 and near SPs 5 and 6) are on opposite sides of the synchrotron ring and that activated air from the shutter voids enters the synchrotron room nearer SPs 5 and 6 than SPs 0 and 9.

And it is noticeable in Table 3 that specific activities of both  $^{11}\text{C}$  and  $^{41}\text{Ar}$  in the air are smaller for air sampled from near SPs 0 and 9 than for air sampled from near SPs 5 and 6, and that ratios of specific activity fall essentially into two sets, the  $^{11}\text{C}$ -to- $^{41}\text{Ar}$  ratio for air sampled from near SPs 0 and 9 SPs 5 and 6 being smaller than the  $^{11}\text{C}$ -to- $^{41}\text{Ar}$  ratio for air sampled from near SPs 5 and 6. These differences may be due to the activated air ‘spreading out’ as it is circulated through the synchrotron room.

#### 4. Minor radionuclides

In order to see the relatively weak lines corresponding to minor radionuclides in the gamma-ray spectra, it is necessary to sum the gamma-ray spectra within each of the ten sets of gamma-ray spectra listed in Table 1 in order to achieve sufficiently good statistics. For each set of gamma-ray spectra, the consistency of the energy scales amongst the individual gamma-ray spectra in the set was checked by forming the standard deviation of the central energies of the 511-keV peaks therein. All such standard deviations were less than 0.1 keV, and so, since the spectrum channel width is 0.25 keV, within each set all the individual spectra could simply be summed. A typical summed spectrum is shown in Fig. 10. The ‘off-the-scale’ peaks are from  $^{11}\text{C}$  and  $^{13}\text{N}$  at 511 keV, and from  $^{41}\text{Ar}$  at 1294 keV.

Peaks in the summed spectra were located using a long-established method [18] based on the smoothed second derivative of the spectrum, and the area of each peak was obtained by fitting [19] a gaussian lying on a straight-line background. Uncertainties in fitted parameters were obtained by perturbing one hundred times the contents  $C_i$  of each channel  $i$  by amounts chosen from random gaussian distributions with standard deviations  $C_i^{1/2}$ , and then taking the standard deviations of the one hundred perturbed values of the parameters. The systematic variation of peak full width at half maximum  $w_{\text{FWHM}}$  as a function of gamma-ray energy  $E_\gamma$  was established by assuming  $w_{\text{FWHM}}^2 = a_0 + a_1 E_\gamma$  and obtaining  $a_0$  and  $a_1$  from a fit to the FWHM values obtained from the gaussian-on-background fits to all the peaks in the summed spectra.

When weak peaks are being looked for in a spectrum, it is obviously important that the energy scale be well established. To check this, twelve readily and reliably identifiable lines in the spectra were used as ‘calibration’ lines, and these are listed in Table 5. The deviations  $\Delta E$  between the apparent energies  $E_{\text{app}}$  of these peaks as they appeared in the summed spectra and the true energies  $E_{\text{tru}}$  given in Table 5 were fitted by the quadratic  $\Delta E = E_{\text{tru}} - E_{\text{app}} = a_0 + a_1 E_{\text{app}} + a_2 E_{\text{app}}^2$  in energy, and the parameters of the fit, and the root-mean-square deviations between the true energies  $E_{\text{tru}}$  and the corrected apparent energies  $E_{\text{app}} + \Delta E$ , are listed in Table 6. It can be seen that after correction energies of measured peaks can be assumed to be good to within  $\sim 0.1$  keV.

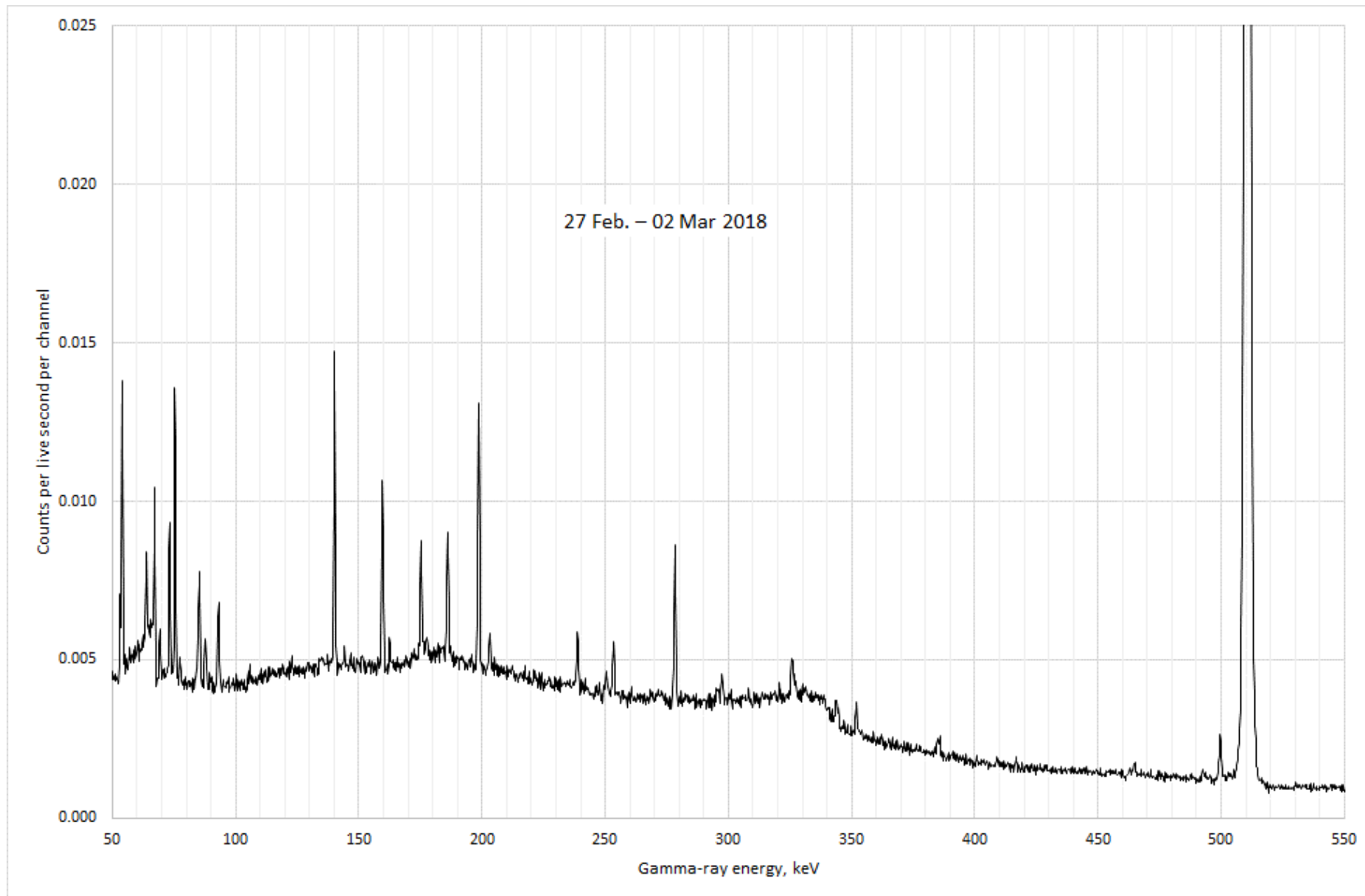


Fig. 10 (part 1 of 4). Sum of 245 individual 900-seconds-long gamma-ray spectra of activated ISIS synchrotron room air.

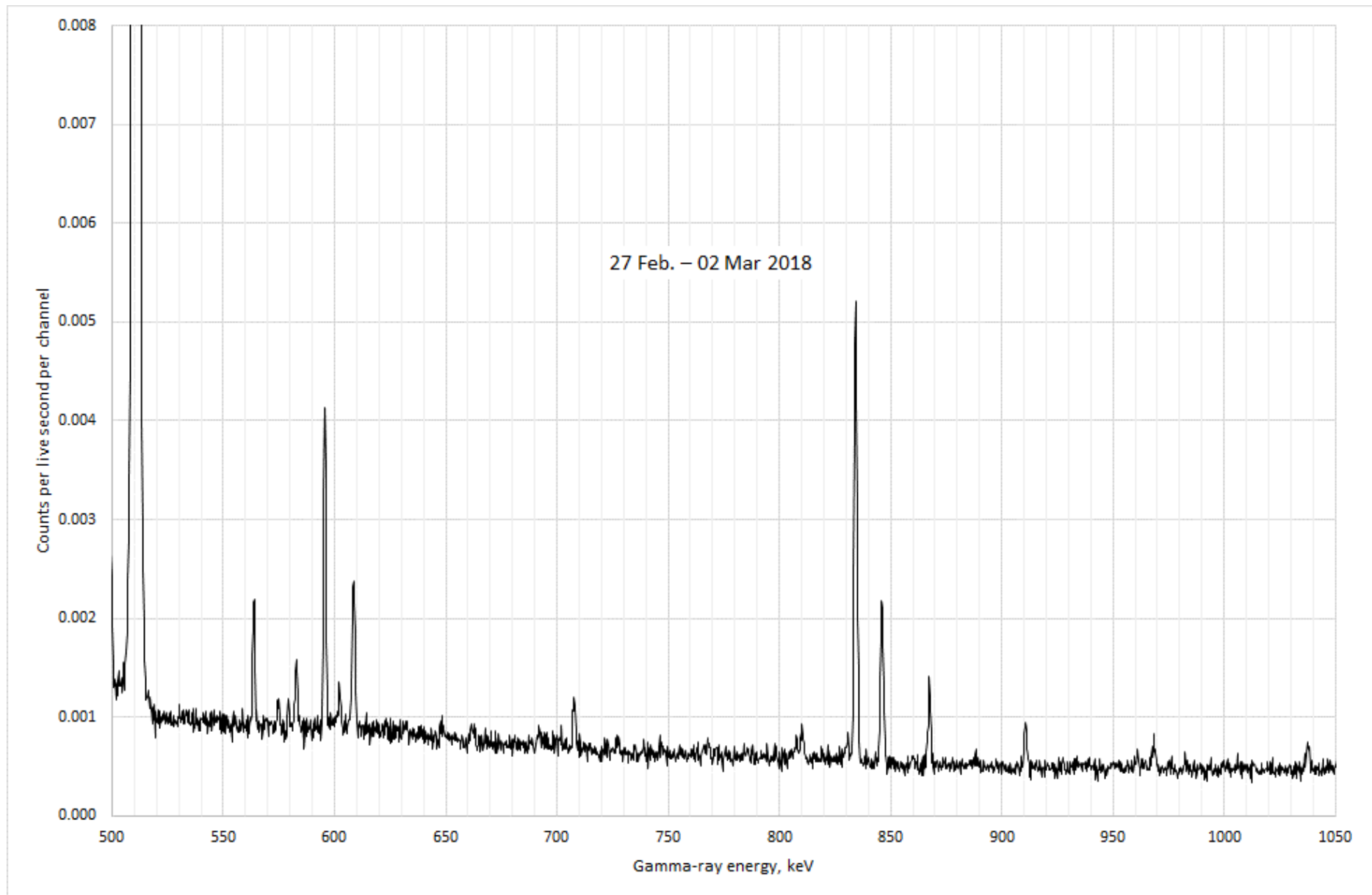


Fig. 10 (part 2 of 4). Sum of 245 individual 900-seconds-long gamma-ray spectra of activated ISIS synchrotron room air.

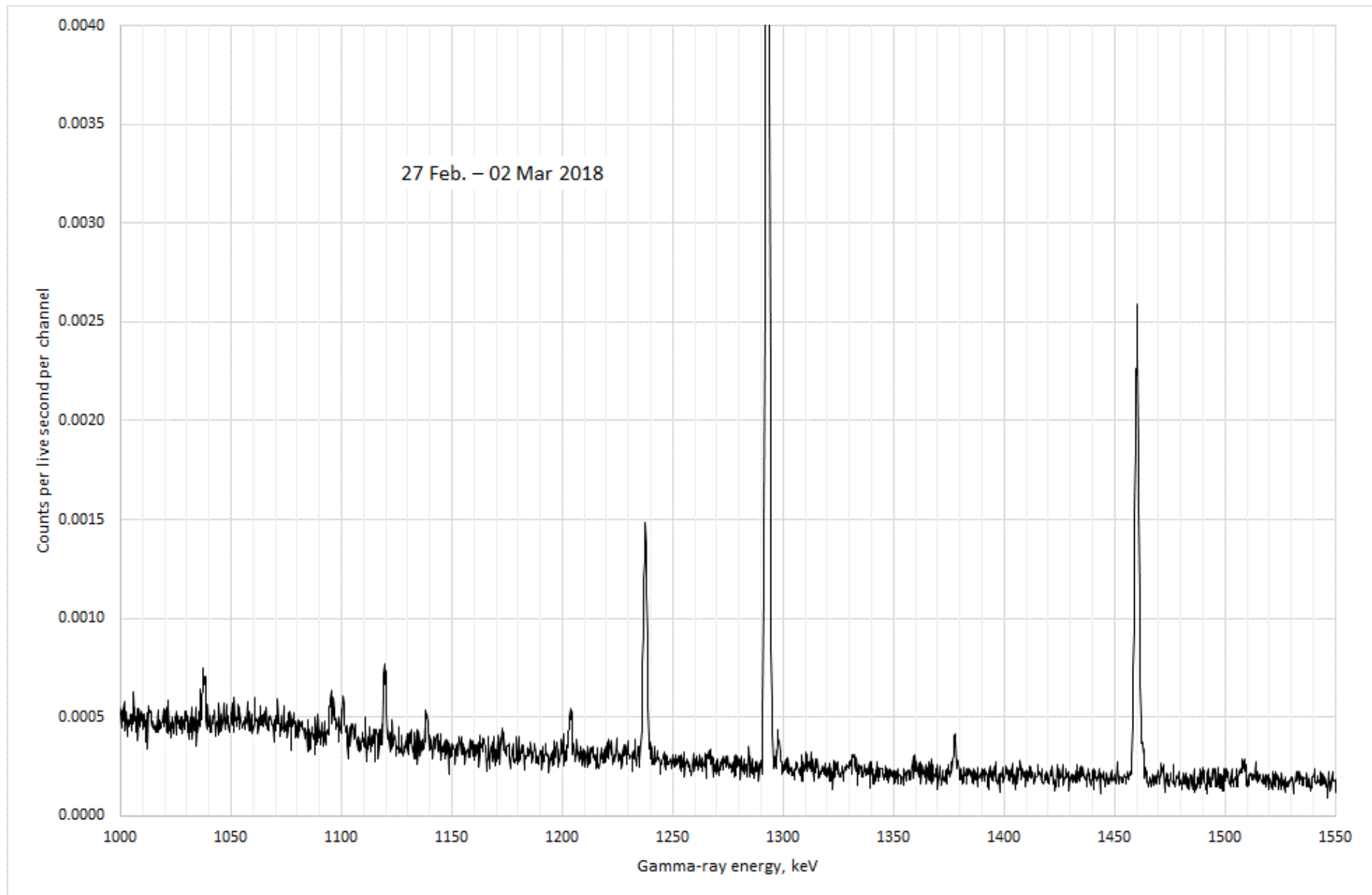


Fig. 10 (part 3 of 4). Sum of 245 individual 900-seconds-long gamma-ray spectra of activated ISIS synchrotron room air.

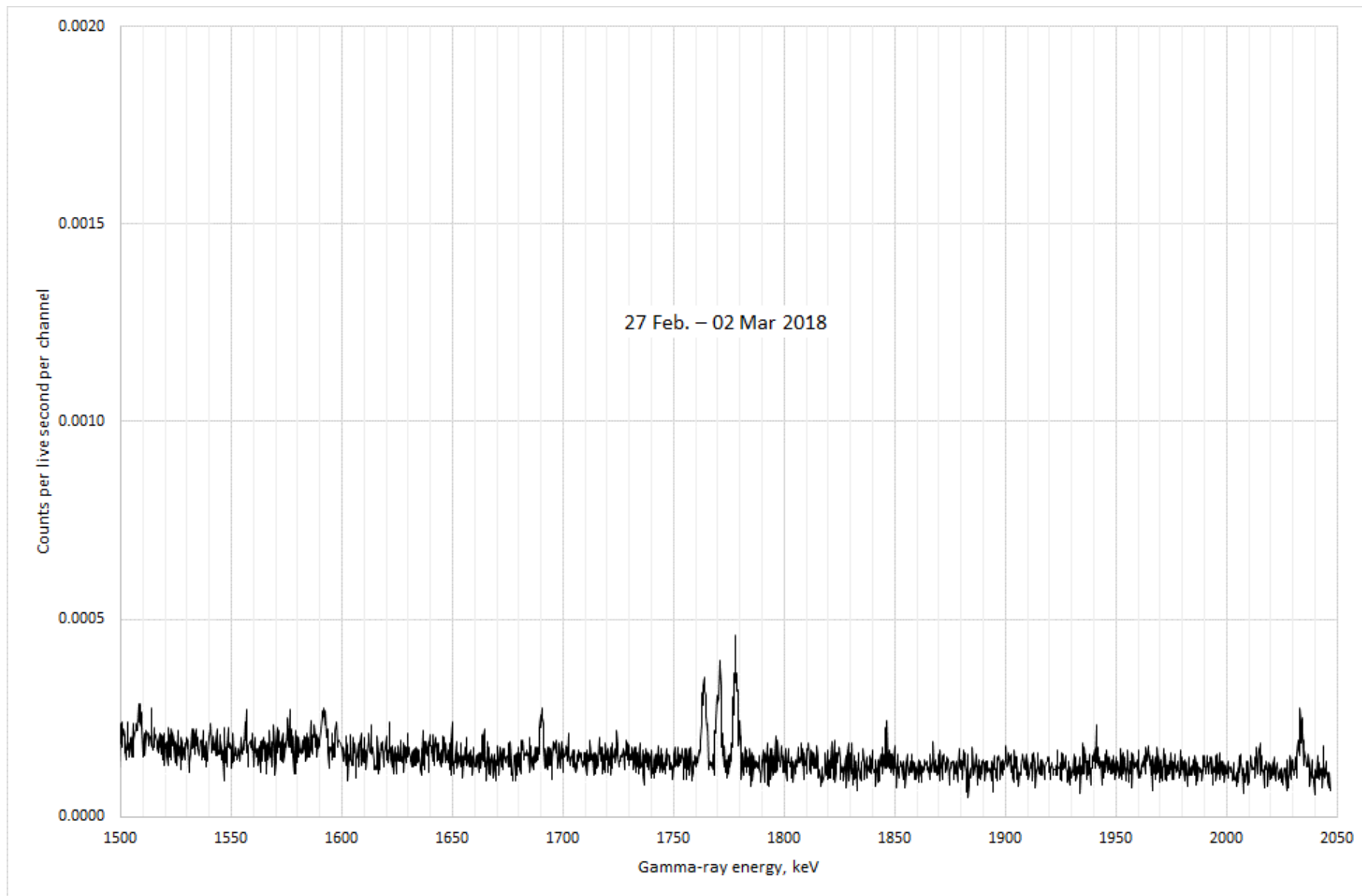


Fig. 10 (part 4 of 4). Sum of 245 individual 900-seconds-long gamma-ray spectra of activated ISIS synchrotron room air.

Line	keV	Origin
Pb K $\alpha_2$	72.804	X-ray fluorescence, lead shielding
Pb K $\alpha_1$	74.969	X-ray fluorescence, lead shielding
Pb K $\beta_{1+3}$	84.769	X-ray fluorescence, lead shielding
Pb K $\beta_2$	87.367	X-ray fluorescence, lead shielding
Pb-212	238.63	Natural terrestrial background
511 keV	511.00	$^{11}\text{C}$ , $^{13}\text{N}$ $\beta^+$ annihil., cosmic rays
Tl-208	583.19	Natural terrestrial background
Bi-214	609.32	Natural terrestrial background
Bi-212	727.33	Natural terrestrial background
Ar-41	1293.64	$^{40}\text{Ar}(n, \gamma)$
K-40	1460.82	Natural terrestrial background
Bi-214	1764.49	Natural terrestrial background

Table 5. X-ray and gamma-ray lines used for checking energy calibration of the HPGe detector system. X-ray line energies were taken from Kaye and Laby [20], X-ray relative strengths were taken from Atomic Data and Nuclear Data Tables [21], and gamma-ray energies were taken from ENDF/B-VII [22].

	# matches	$a_0$	$a_1$	$a_2$	RMS deviation, keV
Feb. 2018	12	-0.567	2.06E-03	-7.73E-07	0.139
Mar. 2018	12	-0.596	2.15E-03	-7.70E-07	0.028
May 2018	12	-0.587	1.59E-03	-8.59E-07	0.092
Jul. 2018	12	-0.594	1.99E-03	-8.91E-07	0.084
Oct. 2018	12	-0.112	1.18E-03	-7.11E-07	0.054
Dec. 2018	12	-0.135	1.91E-03	-8.75E-07	0.083
Apr. 2019	12	-0.134	1.67E-03	-7.80E-07	0.095
Oct. 2019	5	-0.162	1.71E-03	-8.11E-07	0.002
Dec. 2019	12	-0.284	2.05E-03	-9.19E-07	0.041
Feb. 2020	12	-0.009	-1.65E-05	-2.32E-07	0.068

Table 6. Parameters of fits to corrections to apparent energies of peaks in measured summed gamma-ray spectra, and the RMS deviations between the true and corrected apparent energies. Only five ‘calibration’ lines were matched in the October 2019 summed spectrum because these data comprised only six individual 15-minute gamma-ray spectra.

#### 4.1 Specific activities, minor radionuclides

Table 7 lists the count rates for the minor radionuclides  $^7\text{Be}$ ,  $^{38}\text{Cl}$ ,  $^{39}\text{Cl}$  and  $^{40}\text{Cl}$  in activated air from the ISIS synchrotron room ( $^7\text{Be}$  from spallation of nitrogen and oxygen nuclei,  $^{38}\text{Cl}$ ,  $^{39}\text{Cl}$  and  $^{40}\text{Cl}$  from knock-out and charge-exchange reactions in argon). For each  $^7\text{Be}$ ,  $^{38}\text{Cl}$ ,  $^{39}\text{Cl}$  and  $^{40}\text{Cl}$  peak in each summed spectra the count rate was obtained by identifying the expected central position of the peak from the energy calibration procedure already described, attributing to the peak the channels spanning the energy range  $\Delta_{\text{pk}} = 2.2 w_{\text{FWHM}}(E_\gamma)$  symmetrically about the central peak position, and attributing to the background the channels spanning the energy range  $\Delta_{\text{bkg}} = 1.1 w_{\text{FWHM}}(E_\gamma)$  immediately below and above the channels attributed to the

peak<sup>4</sup>. The count rate  $\dot{C}$  was then taken as  $\dot{C} = \{\sum_i P_i - (n/(n' + n''))(\sum_{i'} B_{l,i'} + \sum_{i''} B_{u,i''})\}/t_{\text{live}}$  where the  $P_i$ 's represent the contents of channels in the peak region, the  $B_{l,i'}$ 's and  $B_{u,i''}$ 's represent the contents of channels in the lower and upper background regions,  $n$ ,  $n'$  and  $n''$  are the numbers of channels summed over by  $i$ ,  $i'$  and  $i''$  respectively, and  $t_{\text{live}}$  is the live time. Specific activities  $a$  are also listed in Table 7, and these were obtained from  $a = \dot{C}/(\alpha \varepsilon V)$  where emission probabilities  $\alpha$  were obtained from ENDF/B-VII [22], and absolute full-energy-peak efficiencies  $\varepsilon$  were calculated by integrating the point-source full-energy-peak efficiency of the HPGe gamma-ray detector over the 859-cm<sup>3</sup> volume  $V$  of air seen by the detector.

	Half-life	keV	Emiss. prob., %	Abs. effic'y	10 <sup>6</sup> × count rate, s <sup>-1</sup>	Specific activity Bq cm <sup>-3</sup>
Be-7	53 days	477.6	10.44	1.18E-02	75 ± 227	0.00007 ± 0.00022
Cl-38	37 mins.	1642.4	33.29	3.14E-03	495 ± 87	0.00055 ± 0.00010
Cl-39	56 mins.	250.3	46.10	2.09E-02	2140 ± 402	0.00026 ± 0.00005
		1267.2	53.60	3.95E-03	749 ± 114	0.00041 ± 0.00006
		1517.5	39.24	3.37E-03	142 ± 91	0.00012 ± 0.00008
Cl-40	81 secs.	643.6	6.72	9.04E-03	558 ± 169	-0.00107 ± 0.00032

Table 7. Count rates and specific activities for <sup>7</sup>Be, <sup>38</sup>Cl, <sup>39</sup>Cl and <sup>40</sup>Cl in activated air from the ISIS synchrotron room. These count rates are averages over nine<sup>5</sup> sets of summed gamma-ray spectra after renormalisation to a reference proton beam current of 200 μA. For <sup>38</sup>Cl, the line at 1642.4 keV is the strongest line with an energy less than the maximum energy (2047 keV) in the measured gamma-ray spectra. For <sup>40</sup>Cl, the line at 643.6 keV is the strongest line to which other radionuclides cannot contribute and also the strongest line with an energy less than the maximum energy in the measured gamma-ray spectra.

## 4.2 Discussion

Whilst the specific activity of <sup>7</sup>Be is consistent with zero, an upper limit for the specific activity could be taken as 0.00022 Bq cm<sup>-3</sup>. From the similarity of the <sup>14</sup>N(p,x)<sup>11</sup>C and <sup>14</sup>N(p,x)<sup>7</sup>Be spallation cross-sections shown in Fig. 11, and from the assumption that cross-sections for neutron-induced and proton-induced spallation are similar, <sup>7</sup>Be is likely to be produced in the air in the target monolith shutter voids at roughly the same rate as <sup>11</sup>C. But since the specific activity of <sup>11</sup>C in the synchrotron room air has been measured as ~0.10 Bq cm<sup>-3</sup> (see Sect. 3.4), the inference is that the HEPA filters in the shutter void ventilation system are removing at least 99% of the <sup>7</sup>Be activity.

The <sup>38</sup>Cl specific activity, 0.00055 ± 0.00010 Bq cm<sup>-3</sup>, is consistent with the spallation cross-section [23] of ~10 millibarns for the production of <sup>38</sup>Cl from <sup>40</sup>Ar and the 0.9% constituent of air that is argon. As already stated, the specific activity from nitrogen and oxygen in the air is ~0.10 Bq cm<sup>-3</sup>, the relevant spallation cross-sections for nitrogen and oxygen are ~5–20 millibarns (see Sect. 3.7), and so the specific activity of

<sup>4</sup> A width of 2.2 × the full width at half maximum of a gaussian located symmetrically about the centre of the gaussian encompasses 99% of the full area under the gaussian.

<sup>5</sup> The summed spectrum for October 2019 was omitted, since the total run-time at only 5400 seconds was far from sufficiently long.

$^{39}\text{Cl}$  could be expected to be  $\sim 0.009 \times \sim(10 \div (5-20)) \times \sim 0.10 = 0.0009 \text{ Bq cm}^{-3}$  — all things considered, not inconsistent with  $0.00055 \pm 0.00010 \text{ Bq cm}^{-3}$ .

The average of the three values of  $^{39}\text{Cl}$  specific activity,  $0.00026 \pm 0.00014 \text{ Bq cm}^{-3}$ , is also roughly consistent with the spallation cross-section [23] of  $\sim 10$  millibarns for the production of  $^{39}\text{Cl}$  from  $^{40}\text{Ar}$ , the 0.9% constituent of air that is argon, the specific activity in air of  $\sim 0.10 \text{ Bq cm}^{-3}$  from nitrogen and oxygen, and the spallation cross-sections for nitrogen and oxygen of  $\sim 5-20$  millibarns — the same  $0.0009 \text{ Bq cm}^{-3}$  as in the immediately preceding paragraph.

Since the half-life of  $^{40}\text{Cl}$  is only 1.35 minutes, it is not surprising that there is little evidence for its presence by the time the air reaches the HPGe detector, as it takes  $\sim 15$  minutes (see Table 2) for activated air from the shutter voids to reach the HPGe detector.

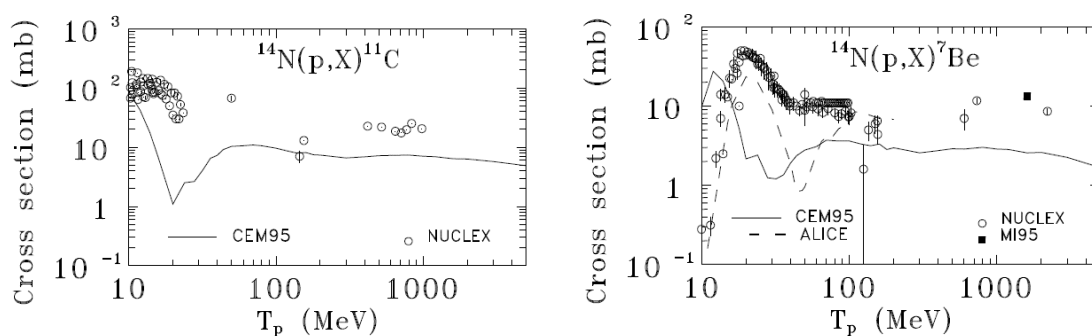


Fig. 11. Comparison of the spallation cross-sections [13] for the production of  $^{11}\text{C}$  and  $^{7}\text{Be}$  from nitrogen, the major component of air. The cross-sections are similar.

## 5. Neutron capture

Readily identifiable gamma-ray lines arising from neutron capture are listed in Table 8. These lines are due to neutrons from the synchrotron room being scattering up the North Tunnel and into R52 where the HPGe gamma-ray detector was situated. Count rates are shown in Fig. 12 and were established as described in Sect. 4.

Overall, the neutron-capture count rates decrease with time, in nice agreement with the general reduction in synchrotron beam losses over the years shown in Fig. 13. The small spike for March 2018 is likely to be due to beam having been delivered to the synchrotron room beam dump (SRBD) on 28 March 2018 thereby leading to anomalously high neutron fluxes within the synchrotron room.

Gamma-ray energy, keV	Reaction	Neutrons captured in
139.7	$^{74}\text{Ge}(n,\gamma)^{75\text{m}}\text{Ge}$	HPGe germanium crystal
198.4	$^{70}\text{Ge}(n,\gamma)^{71\text{m}}\text{Ge}$	HPGe germanium crystal
278.2	$^{63}\text{Cu}(n,\gamma)$	Copper holder, HPGe crystal
595.8	$^{73}\text{Ge}(n,\gamma)$	HPGe germanium crystal
1691.0	$^{123}\text{Sb}(n,\gamma)$	Antimony in lead bricks
1778.8	$^{27}\text{Al}(n,\gamma)$	Aluminium 'snout', HPGe detector

Table 8. Readily identifiable lines in the gamma-ray spectra. Gamma-ray energies from [22, 24, 25].

Three gamma-ray lines, at 835, 847 and 1238 keV, exhibit the anomalous behaviour shown in Fig. 14. It could be thought that these lines are due to  $^{53}\text{Cr}(n,\gamma)$  (neutron capture) and  $^{56}\text{Fe}(n,n'\gamma)$  (neutron inelastic scattering) reactions, but it is surprising that in Fig. 14 the count rates are much higher for the first few months than they are thereafter. In fact, as described in Appendix 3, the most likely explanation is that for the first three measurements in 2018 some activated material was in the neighbourhood of the HPGe detector but outside its surrounding lead shield, but that the activated material was removed before the subsequent measurements were made.

## 6. Uranium-related, thorium-related, and potassium activities

Fig. 15 shows count rates for naturally occurring radioactivity (count rates again established as in Sect. 4). Whilst  $^{208}\text{Tl}$ ,  $^{212}\text{Pb}$  and  $^{214}\text{Bi}$  are decay products of thoron ( $^{220}\text{Rn}$ ) and radon ( $^{222}\text{Rn}$ ), and whilst the spikes in count rates of  $^{208}\text{Tl}$ ,  $^{212}\text{Pb}$  and  $^{214}\text{Bi}$  at March 2018 could in principle be interpreted as spikes in thoron and radon concentrations in air, the fact that the unrelated count rates for  $^{40}\text{K}$  and  $^{228}\text{Ac}$  also exhibit the same behaviour indicate that the spike at March 2018 is most unlikely to be due to a spike in thoron and radon concentrations in air sampled from the synchrotron room. The most likely explanation is that part of the lead shielding around the HPGe gamma-ray detector was not in place during the March 2018 measurements.

Assuming that the March-2018 spike is indeed due to anomalous measurement circumstances, and assuming further that the thoron and radon daughters seen by the HPGe detector bear constant relationships to thoron and radon, the essential constancy of the  $^{208}\text{Tl}$ ,  $^{212}\text{Pb}$  and  $^{214}\text{Bi}$  count rates suggests that the thoron and radon levels around the synchrotron vary little with time—as might well be expected.

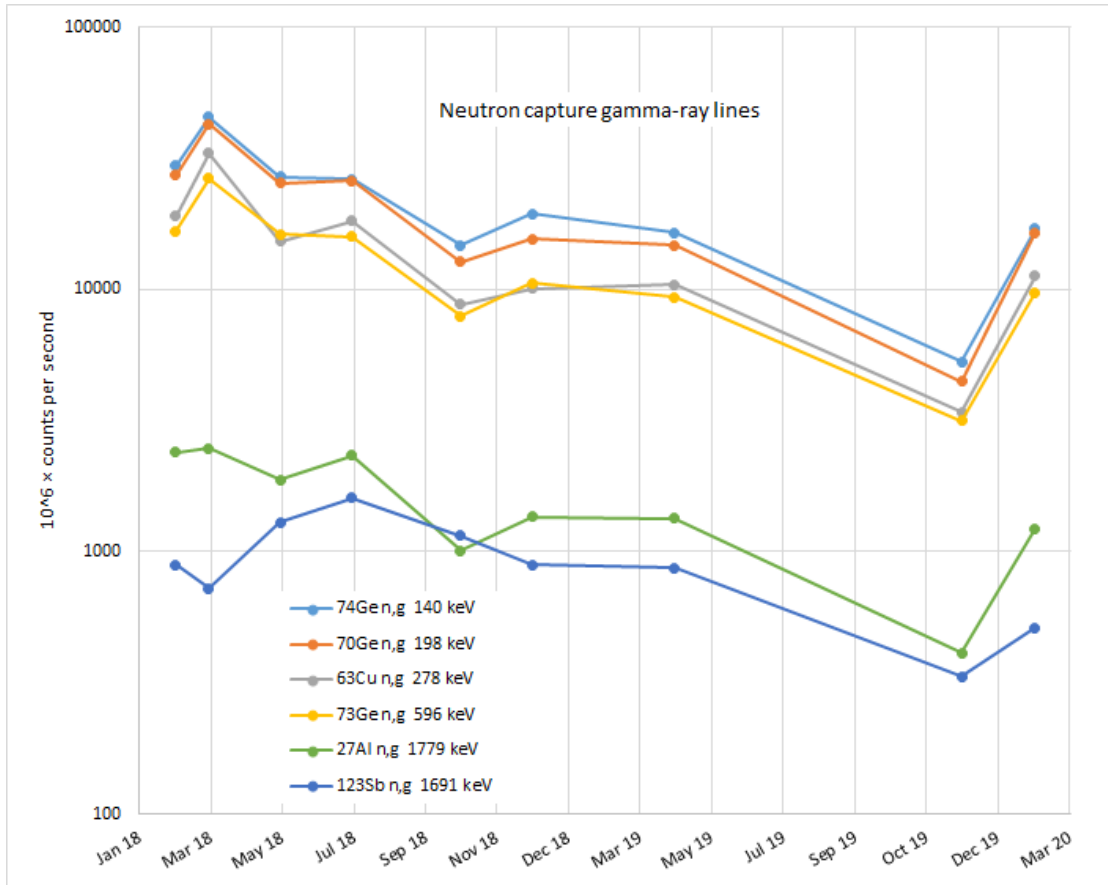


Fig. 12. Count rates for neutron-capture gamma-ray lines ( $'n,g' = (n,\gamma)$ ). As the HPGe gamma-ray detector was always in the same place and in the same configuration, the graphs show neutron fluxes outside the synchrotron room to be decreasing with time, nicely consistent with the general decrease in synchrotron beam losses over time shown in Fig. 13. Capture in  $^{123}\text{Sb}$  arises because lead bricks of the kind used to shield the HPGe gamma-ray detector contain 4% antimony to improve hardness.

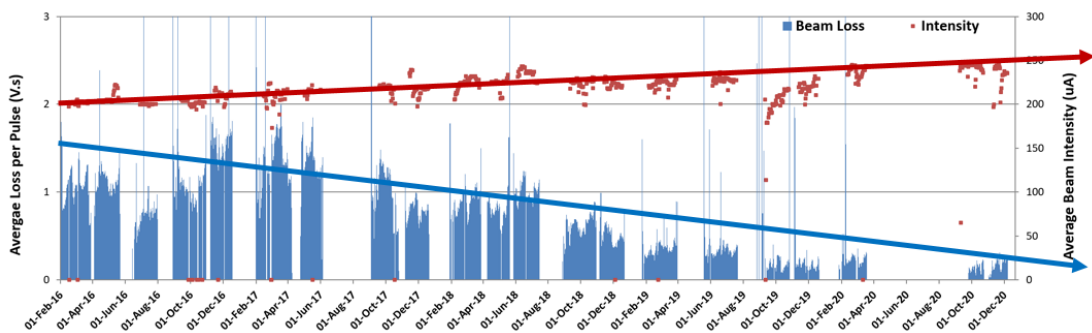


Fig. 13. Synchrotron beam losses as a function of time over some five years [26]. Overall, the beam losses decrease with time, even though the synchrotron beam current increases with time.

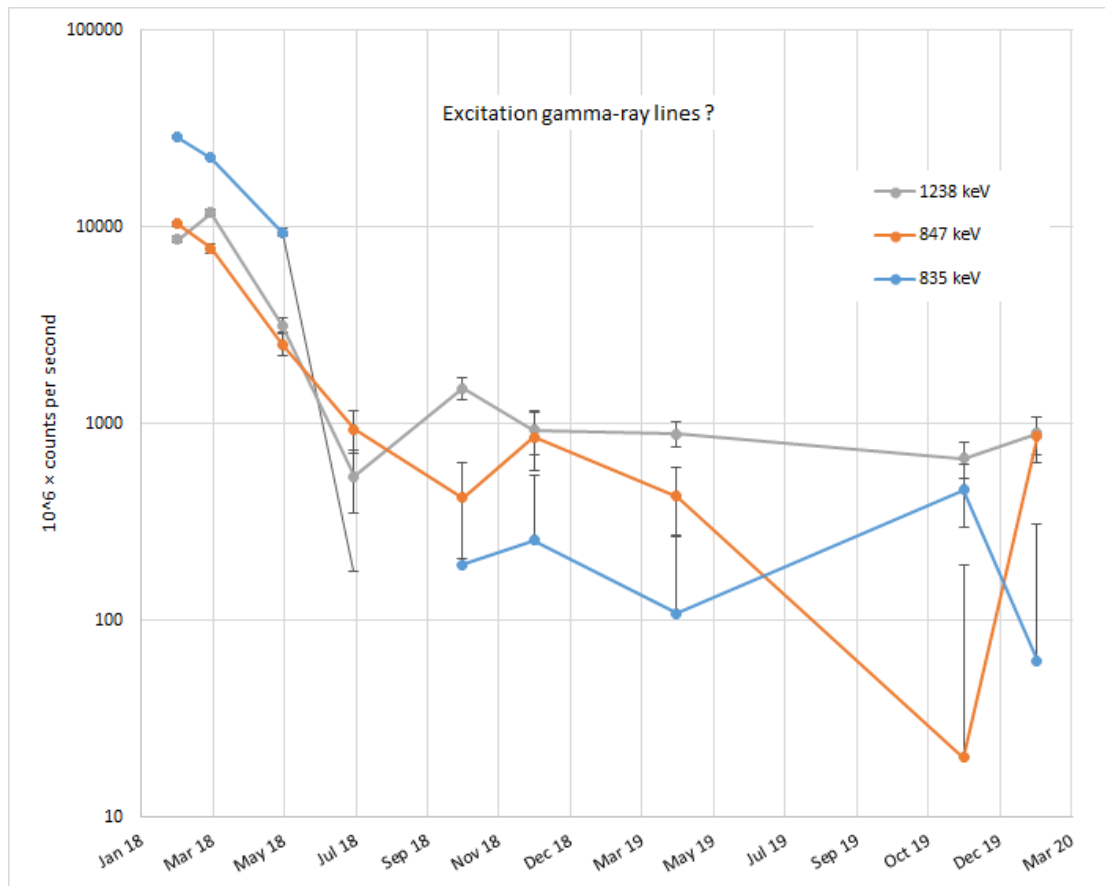


Fig. 14. Count rates for the gamma-ray lines at 835, 847 and 1238 keV.

In the first few months of 2018, radon concentrations within ISIS were measured as part of an independent exercise [27]. Whilst radon measurements in areas exposed to neutrons were not successful, radon levels of  $\sim 30\text{--}40 \text{ Bq m}^{-3}$  were recorded in the catacombs underneath the synchrotron room, and so are likely to be representative of radon levels in the synchrotron room. However, thoron ( $^{220}\text{Rn}$ ) and radon ( $^{222}\text{Rn}$ ) cannot be directly measured by gamma-ray spectroscopy; only the gamma-ray-emitting daughters such as  $^{214}\text{Pb}$  can be so measured, and quantitative results cannot be expected from the present measurements as it is not known whether the daughters remain in the air or, if they do not remain in the air, where and how they are deposited on surfaces. In any case, in the present circumstances, the gamma-ray lines from radionuclides such as  $^{214}\text{Pb}$  seen by the HPGe detector come not from the air in the sample vessel in front of the HPGe detector but from the radium in the concrete surrounding the HPGe detector, as illustrated in Appendix 4.

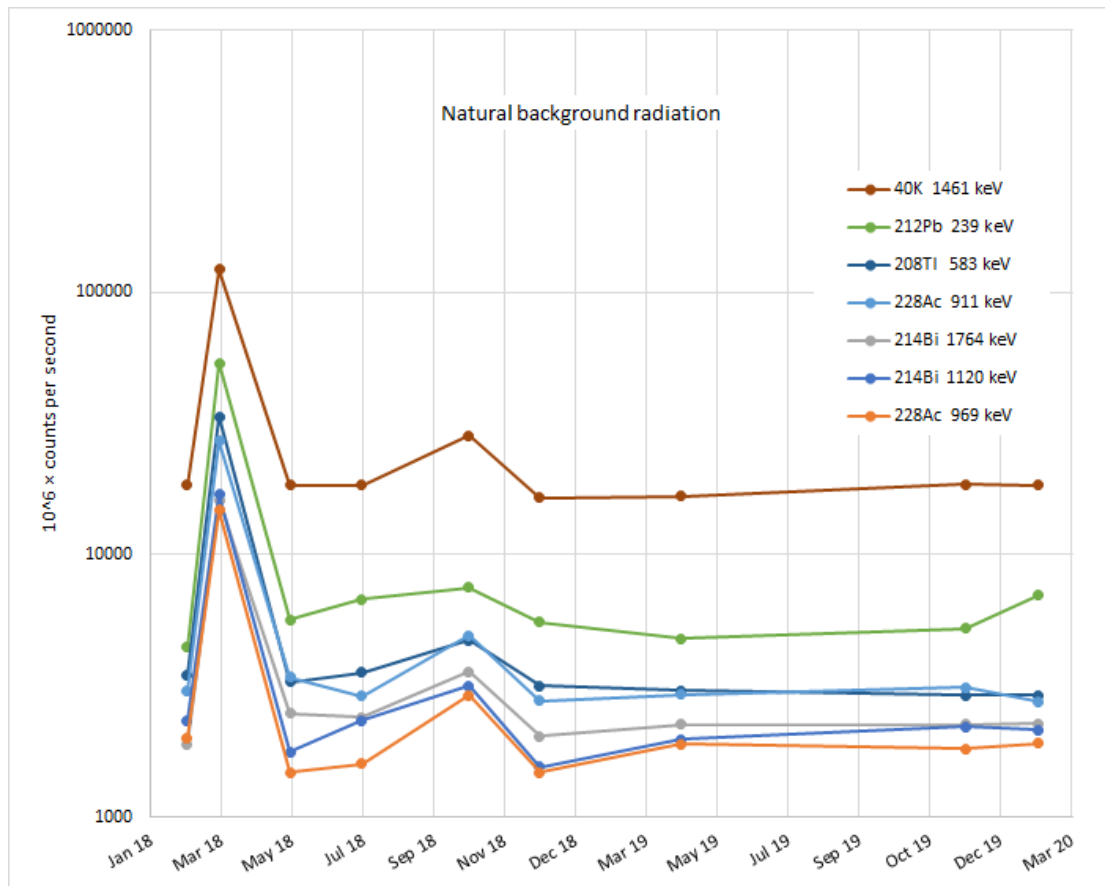


Fig. 15. Count rates for natural background lines. The <sup>40</sup>K and <sup>228</sup>Ac lines are unrelated to radon and thoron activities, since <sup>40</sup>K has nothing to do with the uranium and thorium decay series, and <sup>228</sup>Ac is ‘upstream’ of thoron in the thorium decay chain.

## 7. Neutron interactions in the HPGe detector

In order to extract the most information reasonably possible from the 2363 gamma-ray spectra measured between February 2018 and February 2020, one single good-statistics ‘beam on’ spectrum and one single good-statistics ‘beam off’ spectrum from all the gamma-ray spectra accumulated over the two years were assembled. As described in Sect. 4, one summed gamma-ray spectrum, corrected for the small deviations between apparent and true gamma-ray energies, was produced from each of the ten sets of gamma-ray spectra. However, within the ten sets of spectra the same channel number did not always correspond to exactly the same energy<sup>6</sup>, and so all 2363 individual spectra were re-mapped on to one common set of channel energies 0.25, 0.50, 0.75, ... , 2048.00 keV by linear interpolation. As an overall result, every one of the 2363 individual gamma-ray spectra now had the same channel energies and same energy calibration, and so these 2363 spectra could be combined simply by summing.

In order to suitably combine all these spectra to give one single beam-on spectrum and one single beam-off spectrum, the mean synchrotron beam current was computed from data files in which the synchrotron beam current had been recorded at 4-minute

<sup>6</sup> For example, for the Feb. 2018 summed spectrum the energies of channels 1, 2, 3, ... were 0.65 keV, 0.90 keV, 1.15 keV, ... , whereas for the Feb. 2020 summed spectrum the energies of channels 1, 2, 3, ... were 0.11 keV, 0.36 keV, 0.61 keV, ... .

intervals. All gamma-ray spectra for which the average synchrotron beam current was  $\geq 100 \mu\text{A}$  during the time the spectrum was being accumulated were summed to give the beam-on spectrum, and all gamma-ray spectra for which the average synchrotron beam current was  $< 0.2 \mu\text{A}$  were summed to give the beam-off spectrum. Each of these two summed-counts spectra were then divided by the corresponding sum of live times in order to obtain counts per second. These good-statistics beam-on and beam-off spectra, and, by subtraction, the good-statistics ‘beam on – beam off’ spectrum are shown (in six parts) in Fig. 16. The total run time for the spectra was 28 days.

It is evident, *e.g.* from Fig. 14, that the background varied somewhat with time, and so the background subtraction implicit in Fig. 16 cannot be assumed to be exact. Nevertheless, from an inspection of the spectra in Fig. 16, the distinction between beam-on lines and beam-off gamma-ray lines is nearly always clear.

Peak areas in the three good-statistics spectra were computed automatically and are listed in Table 9. Firstly, as in Sect. 4, peaks in the spectra were identified using a long-established method based on the smoothed second derivative of the spectrum. Secondly, each peak was fitted by a gaussian sitting on a straight-line background, with the peak height, the peak central energy, the peak full width at half maximum (FWHM) and the background underlying the peak all allowed to float. Thirdly, for each of the three spectra, in order to maintain consistency in the variation of peak FWHM with peak energy, especially for weak peaks, the squares of the peak FWHMs were fitted by a linear function of energy<sup>7</sup>. Fourthly, and finally, with the peak central energies established as above and peak FWHMs evaluated from the linear fit, the area of each peak (and the corresponding uncertainty) were obtained by summing over the channels representing the body of the peak and subtracting background established from a few channels on each side of the peak. It should be noted, of course, that strictly this automatic procedure should be applied only to isolated peaks.

---

<sup>7</sup> Note that this systematic behaviour does not represent the FWHM of 511-keV annihilation gamma-ray peaks, which, because of the annihilation of positrons before they have come to rest, is always greater than the FWHM of neighbouring peaks.

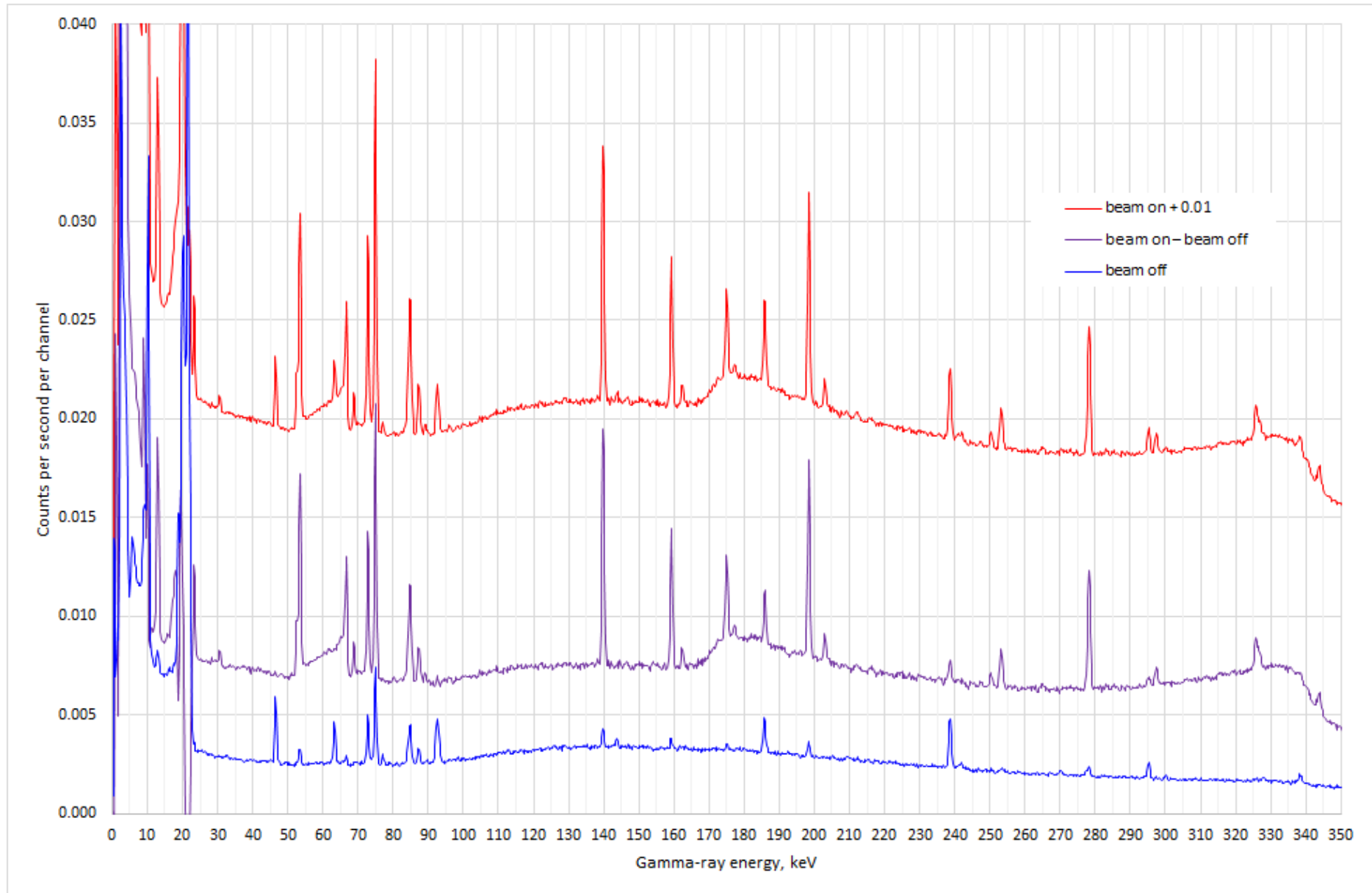


Fig. 16 (part 1 of 6). 'Beam on', 'beam off' and background subtracted 'beam on - beam off' gamma-ray spectra.

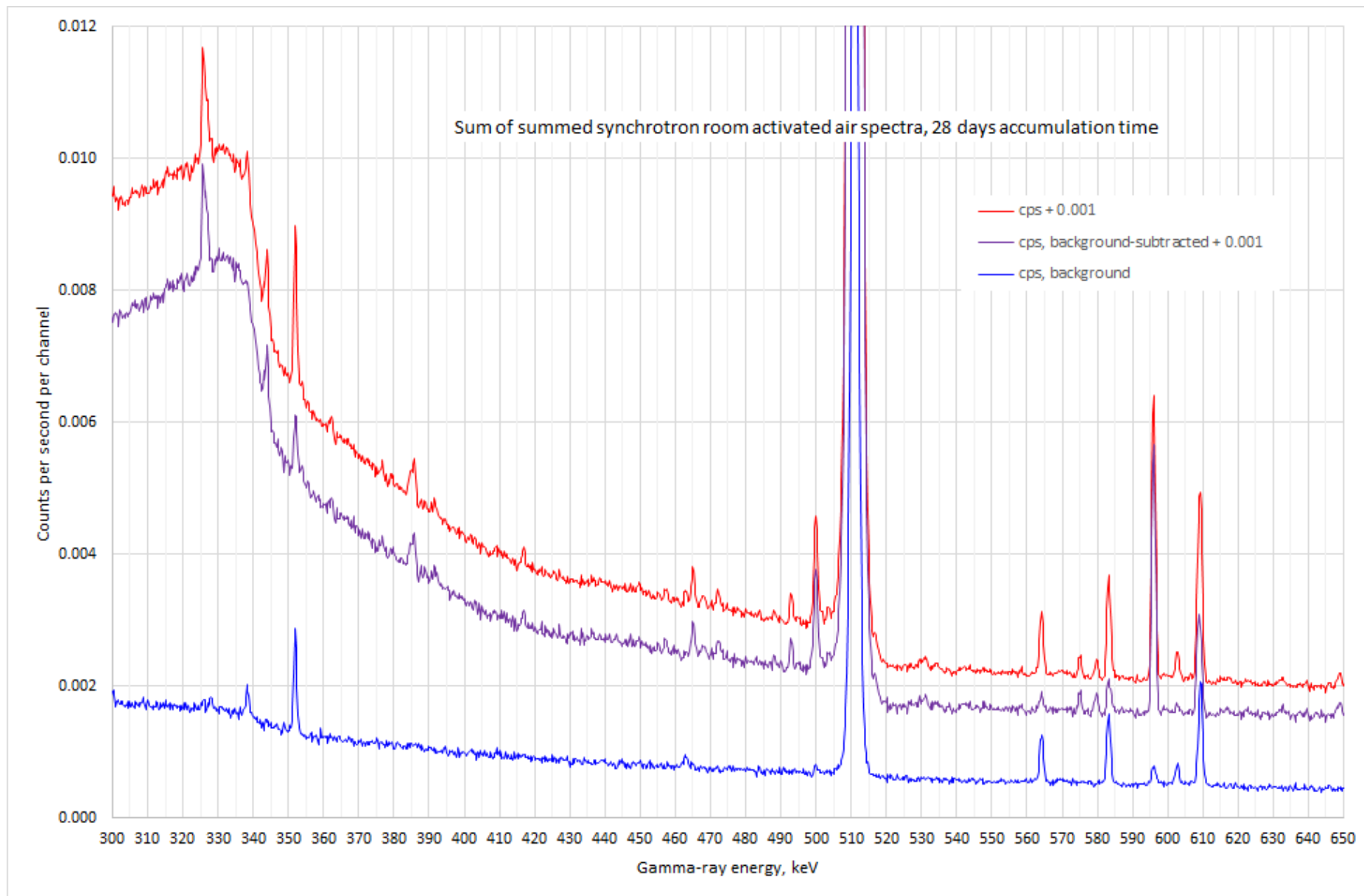


Fig. 16 (part 2 of 6). 'Beam on', 'beam off' and background subtracted 'beam on - beam off' gamma-ray spectra.

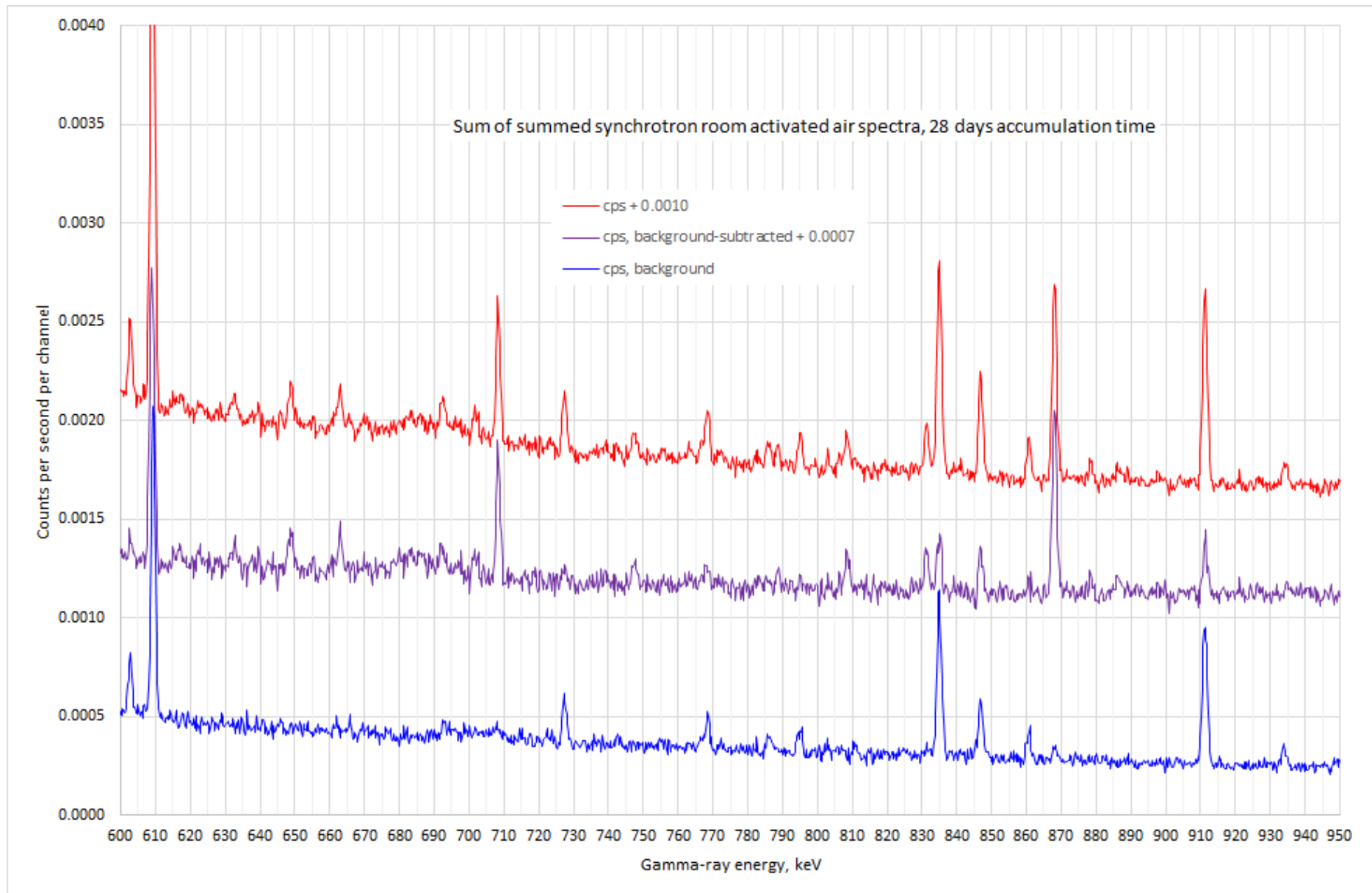


Fig. 16 (part 3 of 6). ‘Beam on’, ‘beam off’ and background subtracted ‘beam on – beam off’ gamma-ray spectra.

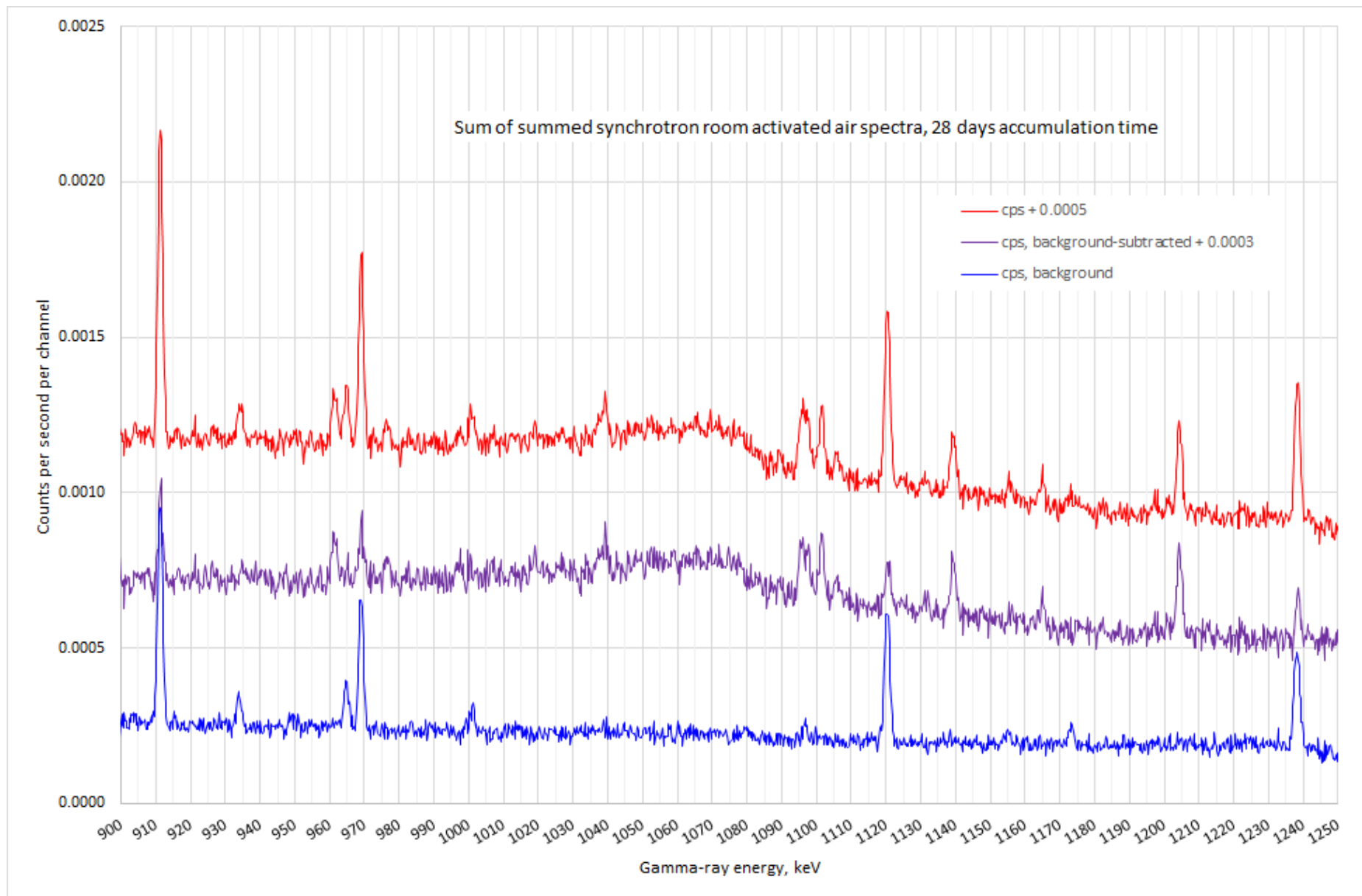


Fig. 16 (part 4 of 6). 'Beam on', 'beam off' and background subtracted 'beam on – beam off' gamma-ray spectra.

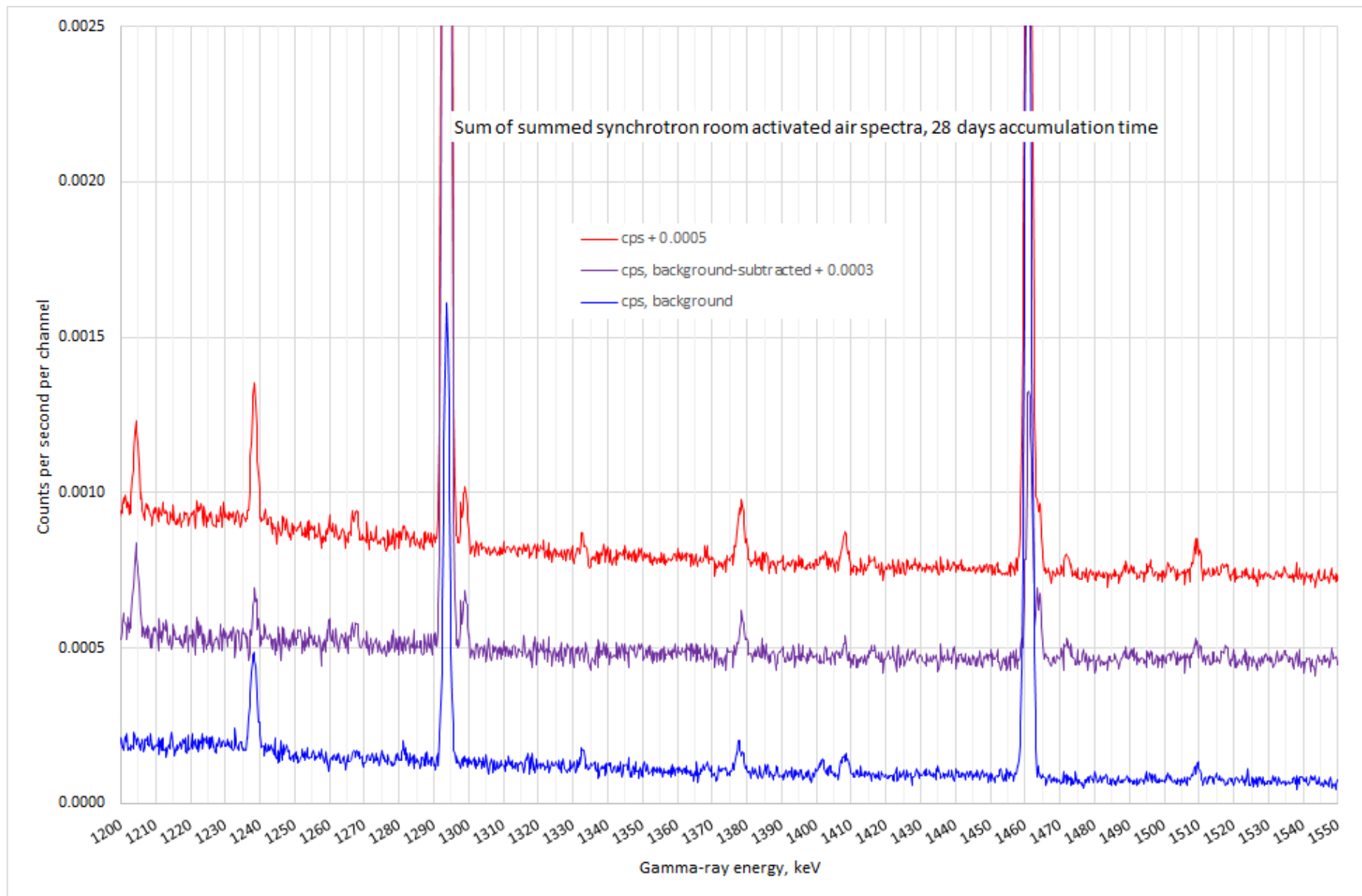


Fig. 16 (part 5 of 6). ‘Beam on’, ‘beam off’ and background subtracted ‘beam on – beam off’ gamma-ray spectra.

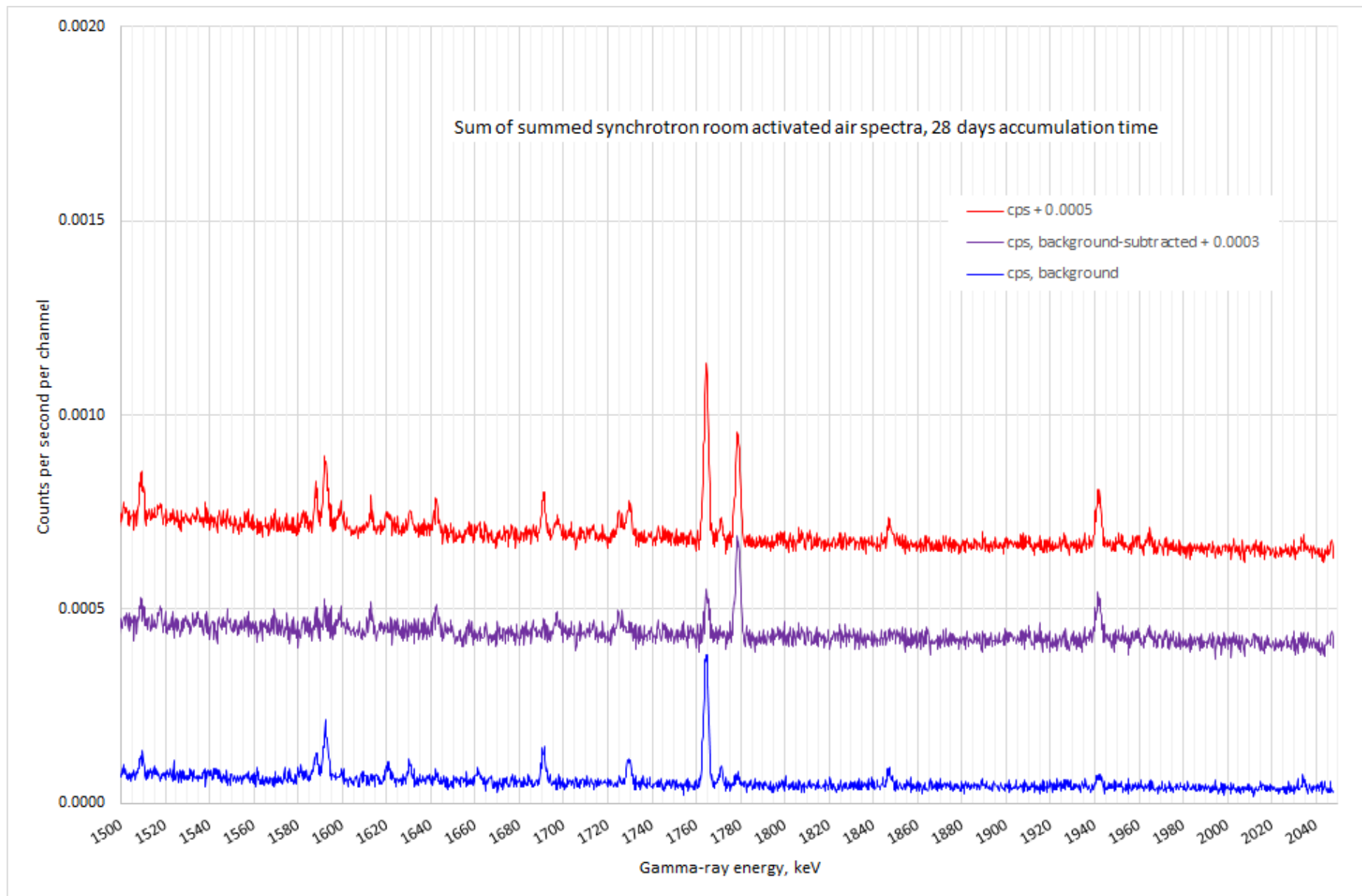


Fig. 16 (part 6 of 6). 'Beam on', 'beam off' and background subtracted 'beam on – beam off' gamma-ray spectra.

keV	foreground	+-	+-keV	background	+-	+-keV	backgnd-subtracted	+-keV
46.53	0.00911	0.00041	0.01	0.00897	0.00026	0.01		
53.42	0.03277	0.00044	0.00	0.00248	0.00026	0.02	0.03322	0.00056
63.31	0.00451	0.00043	0.01	0.00591	0.00028	0.01		0.00
66.59	0.01650	0.00044	0.01	0.00114	0.00026	0.06	0.01281	0.00056
68.82	0.00378	0.00041	0.02				-0.00759	0.00054
72.81	0.02161	0.00043	0.00	0.00500	0.00029	0.01	-0.01325	0.00062
74.97	0.05088	0.00045	0.00	0.01342	0.00030	0.01	0.02021	0.00062
77.10				-0.00020	0.00027	0.04		
84.78	0.02847	0.00041	0.01	0.00830	0.00027	0.01	0.01971	0.00056
87.36	0.00743	0.00040	0.01	0.00230	0.00027	0.02	-0.00071	0.00054
92.61	0.00928	0.00039	0.01	0.00945	0.00029	0.01		
96.07	0.00061	0.00038	0.11					
128.86				0.00051	0.00028	0.23		
139.83	0.03915	0.00049	0.00	0.00274	0.00032	0.02	0.03638	0.00059
143.78	0.00082	0.00045	0.07	0.00090	0.00032	0.08		0.00
146.50	0.00140	0.00047	0.09					
159.28	0.02473	0.00047	0.00	0.00190	0.00031	0.05	0.02242	0.00057
162.38	0.00394	0.00045	0.03				0.00194	0.00054
175.03	0.01444	0.00047	0.01	0.00080	0.00030	0.07	0.01302	0.00065
177.26	-0.00375	0.00046	0.07				-0.01043	0.00065
185.87	0.01572	0.00054	0.01	0.00689	0.00031	0.01	0.00867	0.00062
198.41	0.03637	0.00047	0.00	0.00246	0.00032	0.03	0.03359	0.00061
203.01	0.00514	0.00043	0.02				0.00511	0.00060
212.09	0.00169	0.00047	0.13				0.00182	0.00056
215.93	0.00125	0.00041	6.89				0.00165	0.00055
238.65	0.01280	0.00044	0.01	0.00913	0.00030	0.01	0.00336	0.00055
241.55	0.00207	0.00039	0.14	0.00107	0.00028	0.15		0.05
245.09							-0.00031	0.00052
250.33	0.00262	0.00042	0.04				0.00146	0.00052
253.23	0.00806	0.00039	0.02				0.00646	0.00050
265.00	0.00132	0.00038	0.14				0.00124	0.00049
270.14				0.00096	0.00025	0.13		
278.19	0.02476	0.00043	0.01	0.00213	0.00027	0.07	0.02303	0.00051
295.27	0.00203	0.00040	0.03	0.00299	0.00027	0.02	-0.00190	0.00049
297.43	-0.00002	0.00042	0.03				0.00223	0.00049
300.07				0.00040	0.00023	0.10		
326.09	0.00833	0.00044	0.04	-0.00022	0.00025	0.22	0.00952	0.00053
328.02				0.00051	0.00025	0.14		
338.00	0.00344	0.00045	0.06	0.00201	0.00024	0.05	0.00237	0.00053
343.65	0.00485	0.00036	0.03				0.00367	0.00046
352.00	0.01009	0.00037	0.01	0.00675	0.00023	0.01	0.00371	0.00045
361.83	0.00087	0.00030	0.21				0.00099	0.00040
376.55	0.00047	0.00030	0.11				0.00068	0.00038
385.30	0.00410	0.00031	0.05				0.00361	0.00037
391.37	0.00104	0.00028	5.57				0.00081	0.00035
409.54				0.00041	0.00018	0.21		
416.86	0.00122	0.00025	0.11				0.00099	0.00032
444.71				0.00046	0.00017	1.61		
449.66	0.00030	0.00023	0.26					
457.30	0.00026	0.00025	0.11				0.00017	0.00031
462.94	-0.00129	0.00022	0.18	0.00058	0.00018	0.09		0.14
465.04	0.00142	0.00022	0.04				0.00160	0.00031
467.94	0.00018	0.00022	0.08				-0.00028	0.00028
472.26	0.00121	0.00021	0.11				0.00128	0.00028
493.00	0.00161	0.00021	0.04				0.00163	0.00029
500.04	0.00797	0.00022	0.01	0.00047	0.00016	0.11	0.00807	0.00030
503.73	-0.00157	0.00021	0.13					0.02
511.03	1.70759	0.00156	0.00	0.13511	0.00055	0.00	1.86213	0.00169
521.15				-0.00014	0.00015	0.76		0.00
530.57	0.00122	0.00018	0.18				0.00094	0.00025
534.12	0.00041	0.00017	0.20					1.56
558.38	0.00011	0.00017	0.11				0.00007	0.00023
564.08	0.00514	0.00018	0.02	0.00384	0.00016	0.02	0.00123	0.00025
575.04	0.00125	0.00017	0.04				0.00116	0.00023
579.75	0.00026	0.00017	0.06				0.00125	0.00023
583.28	0.00794	0.00019	0.01	0.00537	0.00017	0.02	0.00262	0.00027
596.01	0.02277	0.00022	0.00	0.00153	0.00015	0.06	0.02117	0.00026
602.74	0.00206	0.00018	0.03	0.00157	0.00015	0.04	0.00049	0.00023
609.12	0.01845	0.00021	0.01	0.00863	0.00018	0.01	0.01014	0.00027
632.37	0.00079	0.00016	0.22					0.02
640.85	-0.00010	0.00015	0.00					
645.91	-0.00060	0.00015	0.16					
648.83	0.00111	0.00015	0.08				0.00133	0.00021
662.93	0.00096	0.00015	0.09				0.00093	0.00020
665.79				0.00028	0.00013	0.11		0.09
692.48	0.00110	0.00016	0.09	0.00036	0.00013	0.63	0.00092	0.00020
701.81	0.00072	0.00016	0.09				0.00051	0.00022
708.31	0.00392	0.00016	0.02				0.00361	0.00021
722.45				0.00026	0.00013	0.19		0.02
727.40	0.00176	0.00015	0.04	0.00145	0.00013	0.07		
742.61	0.00025	0.00015	5.71	0.00030	0.00012	0.19		
747.46	0.00089	0.00015	0.11				0.00070	0.00022
755.71	0.00030	0.00014	0.95					0.27
763.08	0.00030	0.00014	0.15					
768.39	0.00145	0.00016	0.05	0.00091	0.00014	0.07	0.00057	0.00021
772.04	0.00012	0.00014	20.06					0.18
782.71	-0.00006	0.00014	0.22					
786.04	0.00017	0.00014	0.08	0.00059	0.00012	0.27		
788.69	-0.00012	0.00016	0.16				0.00018	0.00020
794.92	0.00095	0.00014	0.06	0.00081	0.00012	0.08		0.14
802.89	0.00021	0.00014	0.11	0.00007	0.00012	0.18		

808.52	0.00062	0.00014	0.09				0.00097	0.00019	0.08
810.83				0.00031	0.00011	0.18			
831.32	-0.00006	0.00016	0.05				0.00048	0.00019	0.07
834.98	0.00659	0.00016	0.01	0.00510	0.00015	0.02	0.00139	0.00023	0.07
846.87	0.00305	0.00015	0.03	0.00165	0.00012	0.04	0.00143	0.00019	0.07
860.67	0.00115	0.00014	0.06	0.00084	0.00012	0.08			
868.11	0.00629	0.00016	0.01	0.00048	0.00012	0.17	0.00580	0.00019	0.01
878.45	0.00056	0.00014	0.10				0.00039	0.00019	0.15
886.14	0.00028	0.00014	0.20				0.00051	0.00019	4.44
911.31	0.00662	0.00016	0.01	0.00496	0.00014	0.02	0.00168	0.00020	0.09
934.10	0.00078	0.00014	0.10	0.00081	0.00012	0.10			
961.39	0.00071	0.00014	0.08				0.00116	0.00020	0.11
964.80	0.00025	0.00014	0.08	0.00047	0.00012	0.07			
969.08	0.00404	0.00015	0.03	0.00262	0.00013	0.03	0.00120	0.00021	0.09
976.47	0.00055	0.00014	0.19				0.00056	0.00017	0.26
997.23							0.00030	0.00017	0.26
1001.00	0.00076	0.00013	0.10	0.00054	0.00011	0.15			
1039.17	0.00079	0.00015	0.14				0.00085	0.00019	0.08
1089.37	0.00013	0.00013	0.19						
1096.49	0.00203	0.00014	0.09	0.00029	0.00011	0.15	0.00168	0.00017	0.20
1101.45	0.00099	0.00013	0.07				0.00079	0.00017	0.08
1105.78	0.00038	0.00013	0.17				0.00023	0.00017	0.37
1120.43	0.00433	0.00015	0.02	0.00323	0.00012	0.02	0.00120	0.00019	0.17
1131.28							0.00034	0.00016	5.34
1139.35	0.00143	0.00013	0.06				0.00142	0.00016	0.09
1155.26	0.00033	0.00012	0.18	0.00038	0.00010	0.33			
1164.95	0.00062	0.00012	0.15				0.00059	0.00016	0.17
1173.20				0.00038	0.00010	0.12			
1182.15	0.00016	0.00012	7.00						
1197.39	0.00017	0.00012	0.26						
1204.35	0.00180	0.00013	0.03				0.00175	0.00016	0.04
1222.46	0.00012	0.00012	0.47				0.00008	0.00015	0.25
1238.33	0.00317	0.00013	0.02	0.00266	0.00012	0.04	0.00058	0.00017	0.08
1247.19	0.00012	0.00010	0.94	0.00007	0.00010	0.24			
1260.14	0.00022	0.00011	1.22				0.00033	0.00014	0.10
1267.26	0.00059	0.00011	0.11	0.00024	0.00009	0.36	0.00022	0.00014	0.19
1281.25				0.00028	0.00009	0.16			
1293.66	0.10336	0.00032	0.00	0.01178	0.00016	0.01	0.09187	0.00036	0.00
1298.75	-0.00313	0.00013	0.05				-0.00632	0.00017	0.07
1332.65	0.00054	0.00010	0.15	0.00021	0.00008	0.11			
1368.21	0.00035	0.00010	0.26	0.00022	0.00007	0.18			
1373.10				-0.00026	0.00008	0.35			
1378.28	0.00173	0.00010	0.06	0.00083	0.00008	0.12	0.00101	0.00013	0.11
1385.48				-0.00006	0.00008	0.31			
1401.47				0.00028	0.00008	0.18			
1408.16	0.00079	0.00009	0.08	0.00051	0.00008	0.07	0.00028	0.00012	0.26
1416.03	0.00034	0.00009	3.10				0.00036	0.00011	0.63
1460.99	0.03239	0.00020	0.01	0.02734	0.00021	0.01	0.00569	0.00029	0.04
1472.06	0.00047	0.00009	0.14				0.00049	0.00011	0.18
1495.83	0.00023	0.00009	0.25						
1501.40	0.00021	0.00009	15.94	0.00006	0.00006	0.33			
1509.25	0.00072	0.00009	0.06	0.00035	0.00007	0.11	0.00040	0.00012	0.25
1517.41	0.00021	0.00009	0.23				0.00025	0.00011	0.27
1542.78				0.00003	0.00007	0.43			
1548.15							0.00005	0.00011	0.19
1580.98				0.00019	0.00006	3.71			
1588.74	-0.00013	0.00010	0.07	-0.00021	0.00008	0.12	0.00010	0.00013	0.00
1592.32	0.00131	0.00009	0.06	0.00091	0.00008	0.07	0.00017	0.00013	0.15
1599.01	0.00047	0.00009	0.24				0.00027	0.00011	6.20
1612.90	0.00036	0.00008	0.21				0.00055	0.00011	5.99
1620.54	0.00028	0.00008	0.20	0.00039	0.00006	0.17			
1630.68	0.00040	0.00009	0.18	0.00032	0.00006	0.21			
1642.46	0.00063	0.00009	0.12	0.00003	0.00006	0.26	0.00060	0.00010	0.26
1661.35	0.00004	0.00008	0.69	0.00026	0.00006	0.27			
1666.67				0.00002	0.00006	0.25			
1690.98	0.00087	0.00009	0.08	0.00076	0.00006	0.07			
1697.10	0.00040	0.00008	0.22				0.00040	0.00011	0.30
1713.21	0.00016	0.00008	0.51				0.00015	0.00010	0.40
1724.99	0.00016	0.00009	0.22				0.00040	0.00010	0.14
1729.52	0.00056	0.00008	0.12	0.00061	0.00006	0.11			
1764.53	0.00413	0.00010	0.02	0.00332	0.00009	0.03	0.00086	0.00014	0.16
1771.09	0.00035	0.00008	0.14	0.00027	0.00006	0.14			
1778.71	0.00279	0.00009	0.04	0.00024	0.00006	0.28	0.00262	0.00011	0.05
1810.69	-0.00008	0.00008	0.25						
1847.25	0.00045	0.00008	0.20	0.00036	0.00006	0.14			
1855.45				0.00005	0.00005	0.35			
1925.99	0.00010	0.00008	7.00				0.00016	0.00009	1.75
1941.81	0.00138	0.00009	0.06	0.00036	0.00006	0.18	0.00101	0.00010	0.09
1960.85	-0.00012	0.00008	0.00						
1964.55	0.00032	0.00008	0.52				0.00023	0.00009	1.69
2033.92	0.00024	0.00008	0.35	0.00016	0.00005	0.17			
2034.41	0.00024	0.00008	0.35	0.00016	0.00005	0.17			

Table 9. Areas (counts per second) of the peaks in the three spectra in Fig. 16 derived automatically as described in Sect. 2.2. Sometimes the automatic procedure fails, as is evident from the occasional negative peak areas. Background-subtracted areas are not always exactly equal to the differences of the foreground and background areas, simply because peak areas were obtained separately from the foreground, background, and background-subtracted spectra. Note that strictly this automatic procedure is valid only for isolated peaks.

Identified gamma-ray peaks are listed in Tables 10 and 11. The beam-on gamma-ray lines arise mostly from neutron capture on the germanium nuclei in the HPGe detector crystal, with a few lines from capture on copper (from the copper holder for the germanium crystal), on aluminium (from the HPGe detector ‘snout’), and on iron (from the steel framework holding the lead shielding). The beam-off gamma-ray lines are mostly the expected natural background, except for  $^{122}\text{Sb}$  and  $^{124}\text{Sb}$  arising from neutron capture on the ~4% antimony incorporated in the lead bricks in the shielding around the HPGe detector to improve hardness.

keV	cps	$\pm$ cps	Identification
53.42	0.03322	0.00056	$^{72}\text{Ge}(\text{n},\text{g})$
66.59	0.01281	0.00056	$^{72}\text{Ge}(\text{n},\text{g})^{73\text{m}}\text{Ge}$
74.97	0.02021	0.00062	Pb X-ray
84.78	0.01971	0.00056	Pb X-ray
87.36	-0.00071	0.00054	Pb X-ray
139.83	0.03638	0.00059	$^{74}\text{Ge}(\text{n},\text{g})^{75\text{m}}\text{Ge}$
159.28	0.02242	0.00057	$^{63}\text{Cu}(\text{n},\text{g})$
175.03	0.01302	0.00065	$^{70}\text{Ge}(\text{n},\text{g})$
185.87	0.00867	0.00062	$^{65}\text{Cu}(\text{n},\text{g}) + ^{226}\text{Ra}$
198.41	0.03359	0.00061	$^{70}\text{Ge}(\text{n},\text{g})^{71\text{m}}\text{Ge}$
203.01	0.00511	0.00060	$^{63}\text{Cu}(\text{n},\text{g})$
253.23	0.00646	0.00050	$^{74}\text{Ge}(\text{n},\text{g})$
278.19	0.02303	0.00051	$^{63}\text{Cu}(\text{n},\text{g})$
297.43	0.00223	0.00049	$^{72}\text{Ge}(\text{n},\text{g})$
326.09	0.00952	0.00053	$^{72}\text{Ge}(\text{n},\text{g})$
343.65	0.00367	0.00046	$^{63}\text{Cu}(\text{n},\text{g})$
352.00	0.00371	0.00045	$^{56}\text{Fe}(\text{n},\text{g})$
385.30	0.00361	0.00037	$^{65}\text{Cu}(\text{n},\text{g})$
465.04	0.00160	0.00031	$^{58}\text{Ni}(\text{n},\text{g}), ^{65}\text{Cu}(\text{n},\text{g})$
472.26	0.00128	0.00028	$^{27}\text{Al}(\text{n},\text{a})^{24}\text{Na}$
500.04	0.00807	0.00030	$^{70}\text{Ge}(\text{n},\text{g})$
511.03	1.86213	0.00169	Annihil. g's
575.04	0.00116	0.00023	$^{74}\text{Ge}(\text{n},\text{g})$
596.01	0.02117	0.00026	$^{73}\text{Ge}(\text{n},\text{g})$
602.74	0.00049	0.00023	$^{123}\text{Sb}(\text{n},\text{g})$
609.12	0.01014	0.00027	$^{63}\text{Cu}(\text{n},\text{g})+^{214}\text{Bi}$
692.48	0.00092	0.00020	$^{56}\text{Fe}(\text{n},\text{g})$
708.31	0.00361	0.00021	$^{70}\text{Ge}(\text{n},\text{g})$
831.32	0.00048	0.00019	$^{70}\text{Ge}(\text{n},\text{g})$
868.11	0.00580	0.00019	$^{73}\text{Ge}(\text{n},\text{g})$
1293.66	0.09187	0.00036	$^{40}\text{Ar}(\text{n},\text{g})$
1460.99	0.00569	0.00029	$^{40}\text{K}$
1778.71	0.00262	0.00011	$^{27}\text{Al}(\text{n},\text{g})$
1941.81	0.00101	0.00010	$^{40}\text{Ar}(\text{n},\text{n}+2\text{p})^{38}\text{S}$

Table 10. Identifications of some of the lines seen in Fig. 16 ( $\text{g} = \gamma$ ,  $\text{a} = \alpha$ ), and the corresponding count rates, beam on.

keV	cps	±cps	Identification
46.53	0.00897	0.00026	210Pb
63.31	0.00591	0.00028	234Th
72.81	0.00500	0.00029	Pb X-ray
74.97	0.01342	0.00030	Pb X-ray
84.78	0.00830	0.00027	Pb X-ray
92.61	0.00945	0.00029	234Th
185.87	0.00689	0.00031	226Ra
238.65	0.00913	0.00030	212Pb
241.55	0.00107	0.00028	214Pb
295.27	0.00299	0.00027	212Pb
300.07	0.00040	0.00023	212Pb
338.00	0.00201	0.00024	228Ac
352.00	0.00675	0.00023	214Pb
462.94	0.00058	0.00018	228Ac
511.03	0.13511	0.00055	Annihil. g's
564.08	0.00384	0.00016	122Sb
583.28	0.00537	0.00017	208Tl
602.74	0.00157	0.00015	124Sb
609.12	0.00863	0.00018	214Bi
768.39	0.00091	0.00014	214Bi
786.04	0.00059	0.00012	214Pb
794.92	0.00081	0.00012	228Ac
834.98	0.00510	0.00015	54Mn
846.87	0.00165	0.00012	56Co
860.67	0.00084	0.00012	208Tl
911.31	0.00496	0.00014	228Ac
934.10	0.00081	0.00012	214Bi
964.80	0.00047	0.00012	228Ac
969.08	0.00262	0.00013	228Ac
1120.43	0.00323	0.00012	214Bi
1238.33	0.00266	0.00012	214Bi, 56Co
1293.66	0.01178	0.00016	41Ar
1378.28	0.00083	0.00008	214Bi
1408.16	0.00051	0.00008	214Bi
1460.99	0.02734	0.00021	40K
1509.25	0.00035	0.00007	214Bi
1588.74	-0.00021	0.00008	228Ac
1592.32	0.00091	0.00008	208Tl, DE, 2614.51
1690.98	0.00076	0.00006	124Sb
1729.52	0.00061	0.00006	214Bi
1764.53	0.00332	0.00009	214Bi
1771.09	0.00027	0.00006	56Co
1847.25	0.00036	0.00006	214Bi
2034.41	0.00016	0.00005	56Co

Table 11. Identifications of some of the lines in Fig. 16 (DE = double escape), and the corresponding count rates, beam off. Note that normal full-energy-peak detection efficiencies may not be valid for these count rates, since, with the lead shielding around the HPGe detector (Fig. 4), most counts will come from gamma-rays that have entered the detector from the rear.

## 7.1 Neutron energies in R52

From the layout shown in Fig. 3, it would not be unreasonable to suppose that by the time neutrons reach the HPGe gamma-ray detector in R52 they have mostly all been thermalised. This supposition is essentially confirmed by the comparison shown in Fig. 17, wherein is shown part of the gamma-ray spectrum from the present measurement in R52 and the corresponding part of a gamma-ray spectrum measured [28] in R55 (the TS-1 experimental hall) where very small but non-zero fast neutron fluxes are known to be present. One obvious difference is the presence in the R55 spectrum of the peak at 692 keV that is essentially absent<sup>8</sup> from the R52 spectrum, a peak that is due to the  $^{72}\text{Ge}(n, n'\gamma)$  reaction (the inelastic scattering of fast neutrons from the TS-1 monolith involving the first excited state of  $^{72}\text{Ge}$  at 691.6 keV); the absence of a 692-keV peak in the R52 spectrum<sup>9</sup> is consistent with the absence of fast neutrons in R52.

Two other peaks present in the R55 spectrum shown in Fig. 17 but absent from the R52 spectrum are at 718 and 788 keV, the former being due possibly<sup>10</sup> to  $^{10}\text{C}$ , and the latter being due to thermal capture on  $^{35}\text{Cl}$  (presumably in PVC<sup>11</sup> or some such similar plastic in R55 in the vicinity of the HPGe detector).

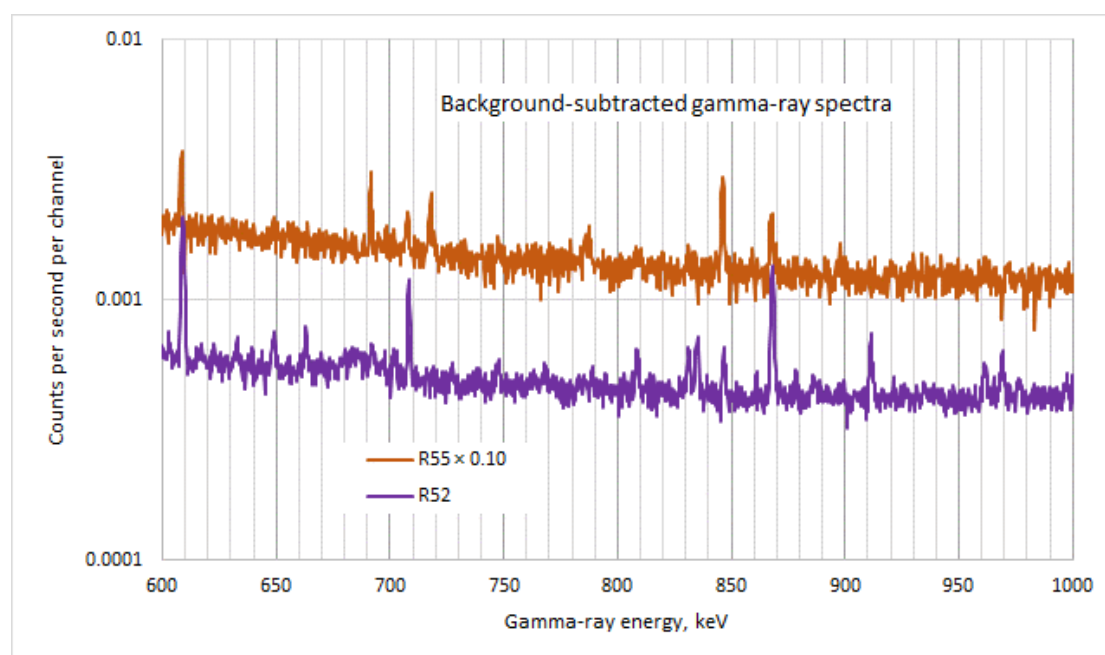


Fig. 17. Comparison of gamma-ray spectra measured in R52 (the work described in the present note) and in R55 in 2013.

<sup>8</sup> The very weak line at 692 keV in the R52 spectra is due to thermal neutron capture on  $^{56}\text{Fe}$ .

<sup>9</sup> The first excited state of  $^{72}\text{Ge}$  cannot be reached by thermal neutron capture, since  $^{71}\text{Ge}$  has a half-life of only 11 days and is therefore absent from the germanium crystal.

<sup>10</sup> The area of the 718-keV peak is  $\sim 0.06\%$  of the area of the 511-keV peak, which is not too different from the ratio of the spallation cross-section for the production of  $^{10}\text{C}$  in air ( $\sim 0.01$  millibarn) and the spallation cross-section for the production of  $^{11}\text{C}$  and  $^{13}\text{N}$  in air ( $\sim 10$  millibarns) [S G Mashnik *et al.*, report LA-UR-97-2905].

<sup>11</sup> There are also lines at 1951 and 1959 keV due to neutron capture on  $^{35}\text{Cl}$  present in the R55 spectrum but absent from the R52 spectrum.

## 7.2 Estimate of thermal neutron flux in R52

As shown by one of the present authors in the 1990s [29], the thermal neutron flux at an HPGe gamma-ray detector can be related to the count rate in the 139.7 keV line arising from neutron capture on  $^{74}\text{Ge}$  in the germanium crystal, the relevant relationships being  $\phi_{th} \cong 980 \dot{C}_{139.7} / \{(\varepsilon_{139.7} + 1.6) V\}$  where  $\phi_{th}$  is the thermal neutron flux ( $\text{cm}^{-2} \text{s}^{-1}$ ),  $\dot{C}_{139.7}$  is the 139.7-keV line count rate ( $\text{s}^{-1}$ ),  $\varepsilon_{139.7}$  is the intrinsic gamma-ray detection efficiency of the HPGe detector at 139.7 keV,  $V$  is the volume of the germanium crystal ( $\text{cm}^3$ ), and  $\varepsilon_{139.7} = 1 - \{1 - \exp(-V^{1/3})\} / V^{1/3}$ . For the Canberra BE3825 HPGe gamma-ray detector used in the present work,  $V = 95 \text{ cm}^3$ , and so, for a 139.7-keV count rate of  $0.036 \text{ s}^{-1}$  (Table 9),  $\phi_{th} = 0.16 \text{ cm}^{-2} \text{ s}^{-1}$ , with an estimated accuracy of  $\pm 30\%$ .

For comparison, the thermal neutron flux in the R52 corridor based on typical beam losses in Straight 1 of the ISIS synchrotron was computed using MORSE [9] and the DLC37F library [10]. The geometry and media used are listed in Table 12. For a neutron source term of  $1.44\text{E}+12$  fission-spectrum neutrons per second<sup>12</sup>, the thermal neutron flux at the position of the HPGe gamma-ray detector in the R52 corridor was<sup>13</sup>  $1.2 \text{ cm}^{-2} \text{ s}^{-1}$ , also with an estimated accuracy (for the statistical component only of the Monte Carlo process) of  $\pm 30\%$ . This is obviously a factor  $\sim 7.6 \pm 3.1$  greater than the value estimated from the gamma-ray spectrum, but hardly unexpectedly different in view of the approximations made in the modelling and the very small probability that a source neutron actually reaches the position of the HPGe detector.

## 8. Radiation dose rates from synchrotron room air

The external radiation dose rate received by a person<sup>14</sup> surrounded by air of uniformly distributed specific activity is  $\dot{H} = a \dot{e}$  where  $\dot{H}$  ( $\text{Sv s}^{-1}$ ) is the dose rate,  $a$  is the concentration of radioactivity ( $\text{Bq m}^{-3}$ ) in the air, and  $\dot{e}$  is the dose rate coefficient for air submersion ( $\text{Sv s}^{-1}$  per  $\text{Bq m}^{-3}$ ).

The equation for the radiation dose rate to a person resulting from the inhalation of a radionuclide that can be absorbed into the body is  $\dot{H} = a e b$  where  $\dot{H}$  ( $\text{Sv s}^{-1}$ ) is the dose rate,  $a$  is the concentration of radioactivity ( $\text{Bq m}^{-3}$ ) in the air,  $e$  is the dose coefficient ( $\text{Sv Bq}^{-1}$ ) relating concentration of radioactivity breathed in to radiation dose delivered (note that  $\dot{e}$  and  $e$  have different units), and  $b$  is the breathing rate ( $\text{m}^3 \text{ s}^{-1}$ ). A commonly used breathing rate is  $20 \text{ litres minute}^{-1}$ , or  $1.2 \text{ m}^3 \text{ hour}^{-1}$  [30].

For inhalation of a radionuclide of an inert (noble) gas that is not absorbed into the body, the relevant equation is  $\dot{H} = a \dot{e}$  where  $a$  is the concentration of radioactivity ( $\text{Bq m}^{-3}$ ) in the air, and  $\dot{e}$  is the dose coefficient ( $\text{Sv s}^{-1}$  per  $\text{Bq m}^{-3}$ ).

---

<sup>12</sup> 5% of 200  $\mu\text{A}$  beam of  $\sim 70$ – $100$  MeV protons lost in the graphite in the collimators in Straight 1, 0.023 neutrons per proton at 85 MeV [IAEA-TRS-283].

<sup>13</sup> This thermal flux was obtained from neutron track lengths in a 10-cm-thick zone encompassing the entire area of the R52 corridor. It had been established, from an ancillary point-detector-mode computation, that within  $\sim \pm 25\%$  Monte Carlo statistics, the thermal neutron flux did not vary significantly across the corridor. It had also been established from an ancillary computation that the lead shielding around the HPGe detector crystal made little difference to the thermal neutron flux seen by the detector (as would be expected from the very existence of lead-slowing-down spectrometers).

<sup>14</sup> It is normally assumed that the person is standing on an uncontaminated flat surface of infinite area.

ID	Type	X	Y	Z	X	Y	Z	X	Y	Z	Description	
0	ISIS synch, homogenised ring, sloping N Tunnel, R52, Str 1 shielding											
RCC	1	0.0	0.0	0.0	0.0	0.0	0.0	820.0	Floor, roof, outer wall of synch room (assume 8 metres high) (100 ft radius) (outer synchrotron area 27 ft high)			
		3048.0										
RCC	2	0.0	0.0	0.0	0.0	0.0	0.0	820.0	Inner wall of synch. room (54 ft radius)			
		1645.0										
RCC	3	0.0	0.0	0.0	0.0	0.0	0.0	820.0	Inner surface of inner synch. area (52 ft radius, assuming 2-ft-thick wall)			
		1585.0										
RCC	4	0.0	0.0	0.0	0.0	0.0	0.0	150.0	Outer surface synch. magnets, RF cavities, etc. 4 feet wide centred on 26 metres radius			
		2660.0										
RCC	5	0.0	0.0	0.0	0.0	0.0	0.0	150.0	Inner surface synch. magnets, RF cavities, etc.			
		2540.0										
BOX	6	-3580.00	640.00	44.4	1145.00	385.00	-88.8	First length of North Tunnel, box sloping upwards				
		-96.85	288.91	7.51	23.57	0.00	303.89	These four boxes from MCGBX3R, MCGBX3 and mcgbx3r.xls				
BOX	7	-4260.00	715.00	97.14	680.00	-75.00	-52.74	Second ..., vertex at height determined by previous upward-sloping box				
		33.31	302.96	-2.58	23.57	0.00	303.89					
BOX	8	-4905.00	1165.00	147.16	645.00	-450.00	-50.02	Third length ..., vertex ...				
		173.88	249.97	-13.49	23.57	0.00	303.89					
BOX	9	-5225.00	1610.00	171.98	320.00	-445.00	-24.82	Fourth length ...				
		246.72	177.95	-19.13	23.57	0.00	303.89					
BOX	10	-6270.00	0.00	178.185	1365.00	1480.00	0.00	R52 corridor, 7 ft x 7 ft x-sec, 178.185 cm above synchrotron floor which is z=0				
		156.84	-144.65	0.00	0.00	0.00	213.36					
BOX	11	-5525.	520.	168.185	-6.691	-7.431	0.	10-cm-wide flux-scoring zone at 42 degrees to x-axis running across corridor, spanning 10 cm below and above corridor and much wider than corridor				
		-453.318	408.170	0.	0.	0.	233.36					
RPP	12	-350.	765.	2180.	2680.	-10.	210.	Inner surface, 2-ft-thick 2-metre high concrete shield around Straight 1				
RPP	13	-410.	825.	2120.	2740.	-20.	200.	Outer surface, 2-ft-thick 2-metre high concrete shield around Straight 1				
RPP	14	-6370.	3148.	-3148.	3148.	-100.	920.	Limit of concrete around everything				
RPP	15	-6470.	3248.	-3248.	3248.	-200.	1020.	Limit of external void				
END												
OUI	OR	1	-2	-4	-13OR	1	12	-4OR	1	12	Synchrotron outer area, incl. inside shielding, north tunnel, and R52 corridor, but not flux-scoring zone	
		5OR	5	-2	-13OR	6OR	7OR	8OR	9OR	10		
		-11										
IN2		3										
RG3		4	-5									
CN4	OR	2	-3OR	14	-1	-6	-7	-8	-9	-10	Synchrotron inner Synchrotron ring, 294.053 m^3 Concrete	
	OR	13	-12	-4OR	13	-12	5					
FX5		11	10									
EX6		15	-14									
END												
1	1	1	1	1	1							
1	1	3	2	1	0							

1=air, 2=concrete, 3=homogenised ring, 4=Pb

Table 12. The outer and inner areas in the ISIS synchrotron room were represented by cylinders, the synchrotron ring was represented by an homogenised mixture of iron and copper, the concrete shielding around Straight 1 was represented by two cuboids, the North Tunnel was represented by four cuboids sloping upwards, and the R52 corridor was represented by a cuboid.

For submersion in activated air and inhalation of activated air in the ISIS synchrotron room, the relevant radionuclides to be considered (see Sect. 3) are  $^{11}\text{C}$  and  $^{41}\text{Ar}$ . From measurements made of 12-GeV-proton activated air at KEK, it was found that essentially 80% of the  $^{11}\text{C}$  in activated air is present as  $^{11}\text{CO}$ , and 20% as  $^{11}\text{CO}_2$  [31]. Dose coefficients are listed in Table 13.

	Dose coefficient [32], adult, submersion in air, Sv Bq <sup>-1</sup> s <sup>-1</sup> m <sup>3</sup>	Dose coefficient [33], inhalation, worker, Sv Bq <sup>-1</sup>	Dose coefficient [34], inert gases, worker, Sv Bq <sup>-1</sup> day <sup>-1</sup> m <sup>3</sup>
$^{11}\text{C}$	4.58E-14		
$^{11}\text{CO}$		1.2E-12	
$^{11}\text{CO}_2$		2.2E-12	
$^{41}\text{Ar}$	6.20E-14		5.3E-09

Table 13. Dose coefficients for  $^{11}\text{C}$  and  $^{41}\text{Ar}$ . In fact, because the inert gas argon is not absorbed into the body, for  $^{41}\text{Ar}$  the second and fourth columns (although given in different units) actually represent the same process and list the same numbers.

From Sect. 3, the specific activities of the air in the ISIS synchrotron room at saturation are  $\sim 0.10 \text{ Bq cm}^{-3}$  and  $\sim 0.03 \text{ Bq cm}^{-3}$  for  $^{11}\text{C}$  and  $^{41}\text{Ar}$  respectively, *i.e.*  $\sim 1 \times 10^5 \text{ Bq m}^{-3}$  and  $\sim 3 \times 10^4 \text{ Bq m}^{-3}$  respectively). Using the dose coefficients from Table 13, these specific activities give rise to the dose rates in Table 14 — in which dose rates from submersion dominate. Once the synchrotron beam has been switched off, dose rates from  $^{11}\text{C}$  and  $^{41}\text{Ar}$  decrease with half-lives of 20 and 110 minutes respectively.

Of course, as is evident from Table 3, there are variations in the specific activity of the air throughout the synchrotron room of factors  $\sim 0.5$ – $2.0$ , but the time for air to be circulated once through the synchrotron room by the air-conditioning system is<sup>15</sup>  $\sim 10$  minutes, and so once ten minutes have elapsed after synchrotron beam switch-off spatial inhomogeneities in air specific activity will have been largely averaged out.

	Specific activity, Bq m <sup>-3</sup>	Submersion		Inhalation		
		Dose coeff., Sv Bq <sup>-1</sup> s <sup>-1</sup> m <sup>3</sup>	Dose rate, $\mu\text{Sv h}^{-1}$	Dose coeff., Sv Bq <sup>-1</sup>	Breath. rate, m <sup>3</sup> h <sup>-1</sup>	Dose rate, $\mu\text{Sv h}^{-1}$
$^{11}\text{C}$	1.0E+05	4.58E-14	16			
$^{11}\text{CO}$	8.0E+04			1.20E-12	1.20	0.12
$^{11}\text{CO}_2$	2.0E+04			2.20E-12	1.20	0.05
$^{41}\text{Ar}$	3.0E+04	6.20E-14	7			

Table 14. Dose rates from activated air at saturation in the ISIS synchrotron room. The specific activities for  $^{11}\text{CO}$  and  $^{11}\text{CO}_2$  are respectively 80% and 20% of the overall  $^{11}\text{C}$  specific activity.

<sup>15</sup> Synchrotron room volume  $\sim 25000 \text{ m}^3$ , air flow speed  $\sim 40 \text{ m}^3 \text{ s}^{-1}$ .

## 9. Summary and conclusions

Between February 2018 and February 2020, measurements were made of the activity of the air in the ISIS synchrotron room using a remote shielded HPGe gamma-ray detector, some two thousand separate gamma-ray spectra being collected.

The main radionuclides found were  $^{11}\text{C}$  and  $^{41}\text{Ar}$ , with less  $^{13}\text{N}$  being seen than expected. Representative values of  $^{11}\text{C}$  and  $^{41}\text{Ar}$  specific activity were  $\sim 0.10$  and  $\sim 0.03 \text{ Bq cm}^{-3}$  respectively. The corresponding submersion dose rates at saturation were estimated as 16 and  $7 \mu\text{Sv hour}^{-1}$  respectively.

The activity in the air in the synchrotron room was deduced to arise primarily from neutron irradiation of ventilation air in the shutter voids in the target monoliths.

Specific activities were also obtained for  $^7\text{Be}$ ,  $^{38}\text{Cl}$ ,  $^{39}\text{Cl}$  and  $^{40}\text{Cl}$ , and the low limit on the specific activity of  $^7\text{Be}$  confirmed the  $>99\%$  efficacy of the HEPA filters in the ventilation systems.

Many gamma-ray lines from neutron interactions were seen, and an estimate of the thermal neutron flux at the position of the HPGe detector was as consistent as could reasonably be expected with a Monte Carlo estimate based on likely neutron production rates in Straight 1 of the synchrotron.

## References

- [1] <https://www.isis.stfc.ac.uk>
- [2] J W G Thomason, Nucl. Instr. Meth. A917 (2019) 61.
- [3] S Karbassi and A Nilsson, ISIS internal report, July 2021.
- [4] D J S Findlay, Appl. Radiat. Isot. 121 (2017) 61.
- [5] National Nuclear Data Center Q-value Calculator, <https://www.nndc.bnl.gov/qcalc/qcalcr.jsp>
- [6] F Burge and G P Škoro, 'Radiation doses from air activation in the ISIS synchrotron', internal ISIS report, 8 October 2012.
- [7] B Jones, S A Fisher and A Pertica, Proc. 10th Int. Particle Accel. Conf., Melbourne, June 2019, p 2701.
- [8] S Karbassi and A Nilsson, ISIS internal report, June 2021.
- [9] N P Taylor and J Needham, 'MORSE-H: A Revised Version of the Monte Carlo Code MORSE', AERE-R 10432, 1982.
- [10] L J Baker and N P Taylor, 'The Harwell Version of the DLC37F Nuclear Data Library', AERE-R 11849, 1985.
- [11] F Burge *et al.*, Nucl. Instr. Meth. A1013 (2021) 165640.
- [12] For example, 'JANIS Book of neutron-induced cross-sections', [https://www.oecd-nea.org/jcms/pl\\_44624/janis-books](https://www.oecd-nea.org/jcms/pl_44624/janis-books)
- [13] S G Mashnik *et al.*, report LA-UR-97-2905.
- [14] D J S Findlay, ISIS internal report, ISIS-DJSF-21-06-B, June 2021.
- [15] R P Morco *et al.*, Corrosion Eng., Sci. Technol., 52 (2017) 141.
- [16] I L Rakhno *et al.*, Nucl. Instr. Meth. B414 (2018) 4.
- [17] A Endo *et al.*, [https://www.researchgate.net/publication/237592652\\_Characterization\\_of\\_11C\\_13N\\_and\\_15O\\_produced\\_in\\_Air\\_through\\_Nuclear\\_Spallation\\_Reactions\\_by\\_High\\_Energy\\_Protons](https://www.researchgate.net/publication/237592652_Characterization_of_11C_13N_and_15O_produced_in_Air_through_Nuclear_Spallation_Reactions_by_High_Energy_Protons)
- [18] G W Phillips and K W Marlow, Nucl. Instr. Meth. 137 (1976) 525.
- [19] Using VA04AD from the Harwell Subroutine Library, <https://www.hsl.rl.ac.uk/>.
- [20] 'Tables of Physical and Chemical Constants', Kaye & Laby, Longman, 16th edition, 1995.
- [21] S I Salem *et al.*, Atom. Data Nucl. Data Tables 14 (1974) 91.
- [22] <http://www.nndc.bnl.gov/endl/b7.1/download.html>
- [23] R L Brodzinski and N A Wogman, Phys. Rev. C1 (1970) 1955.
- [24] J K Tuli, report BNL-NCS-64434, 1997.
- [25] <https://www-nds.iaea.org/capgam/indexbye.htmlx>
- [26] H V Cavanagh, personal communication.

- [27] ISIS RPA Advice Note AN/RAL/18/001.
- [28] F Burge, personal communication. Measurement made in 2013, very probably on the North Balcony opposite the TS-1 target monolith.
- [29] G P Škoro *et al.*, Nucl. Instr. Meth. A316 (1992) 333.
- [30] ICRP P119, Compendium of Dose Coefficients based on ICRP Publication 60, 2012.
- [31] ‘Characterization of  $^{11}\text{C}$ ,  $^{13}\text{N}$  and  $^{15}\text{O}$  produced in Air through Nuclear Spallation Reactions by High Energy Protons’, P-6a-336, A Endo, Y Oki, Y Kanda and K Kondo, KEK, Japan.
- [32] ‘External Exposure to Radionuclides in Air, Water and Soil’, EPA-402/R19/002, August 2019.
- [33] Table B.1, ICRP P119.
- [34] Table C.1, ICRP P119.
- [35] <https://www-nds.iaea.org/relnsd/NdsEnsdf/QueryForm.html>
- [36] <https://physics.nist.gov/PhysRefData/Xcom/html/xcom1.html>
- [37] K Kovler, J. Environmental Radioactivity 168 (2017) 46.
- [38] S Croft and W Russ, ICEM05-1228, 10th Int. Conf. Environm. Remed. Rad. Waste Management, 4–8 September 2005, Glasgow.

## Appendix 1. Count rates in HPGe detector

In order to extract information from sets of data such as the set illustrated in Fig. 6, the following model was adopted. Assume atoms of radionuclides  $i$  are produced by the proton beam at rates  $r_i I$  where  $I$  is the proton beam current and  $r_i$  is a constant of proportionality (atoms  $\mu\text{A}^{-1} \text{s}^{-1}$ ). Suppose activated air takes time  $\delta_s$  to get from wherever it is produced to the synchrotron room. Then in time  $dt$  the number of atoms of radionuclide  $i$  appearing at time  $t$  in the synchrotron room is  $dN_i = \exp(-\lambda_i \delta_s) r_i I(t - \delta_s) dt$  where  $\lambda_i = \ln(2)/t_{1/2,i}$  is the decay constant for radionuclide  $i$  and  $t_{1/2,i}$  is its half-life. Suppose there are  $N_i$  atoms of radionuclide  $i$  in the synchrotron room at time  $t$ , and suppose the air exchange rate and synchrotron room volume are  $v$  ( $\text{m}^3 \text{s}^{-1}$ ) and  $V$  ( $\text{m}^3$ ) respectively. Then, in time  $dt$ ,  $\lambda_i N_i dt$  atoms decay, and  $(v/V) N_i dt$  atoms are removed. So the net change in number of atoms of radionuclide  $i$  in the synchrotron room is  $dN_i = \exp(-\lambda_i \delta_s) r_i I(t - \delta_s) dt - \lambda_i N_i dt - (v/V) N_i dt$ , which may be rewritten as  $dN_i = \exp(-\lambda_i \delta_s) r_i I(t - \delta_s) dt - \lambda'_i N_i dt$  where  $\lambda'_i = \lambda_i + v/V$ . Since  $I = I(t)$  is a known function of time ( $I(t)$  is measured and recorded in 4-minute steps),  $N_i = N_i(t)$  may be obtained by numerical integration, and thereby activities in the synchrotron room  $\lambda_i N_i = \lambda_i N_i(t)$  may be obtained.

Suppose it takes time  $\delta_c$  for the activated air to get from the synchrotron room to the HPGe detector, and assume that the gamma-ray emission probability for radionuclide  $i$  is  $\alpha_i$  and that the HPGe detection efficiency for gamma-rays from radionuclide  $i$  is  $\varepsilon_i$ . Then the number of HPGe counts  $c_{i,j}$  from radionuclide  $i$  over a counting interval  $\Delta$  beginning at time  $t_j$  is  $c_{i,j} = c_i(t_j + \Delta) = \alpha_i \varepsilon_i \int_{t_j}^{t_j + \Delta} \exp(-\lambda_i \delta_c) \lambda_i N_i(t - \delta_c) dt$ . By minimising  $\chi^2_{\text{pdf}} = \{\sum_i (\sum_j (C_{i,j} - B_i - c_{i,j})^2 / \delta C_{i,j}^2)\} / \{mn - (2m + 2)\}$  where  $m$  is the number of radionuclides, parameters  $r_i$ ,  $\delta_s$ ,  $\delta_c$  and  $B_i$  may be extracted, where  $i$  runs from 1 up to  $m$ , the  $C_i$ 's are the measured counts corresponding to radionuclide  $i$ ,  $B_i$  is the corresponding background, and  $j$  runs from 1 up to  $n$  where  $n$  is the number of counting intervals.

If the passage of activated air from the source of production to the synchrotron room is characterised not by a unique time but by a symmetrical distribution of times spanning a finite range  $2w$  described by a normalised function  $s(\varepsilon) = s(\bar{t}, \varepsilon)$  where  $\bar{t}$  is the mean time and  $\varepsilon$  is the deviation from the mean time (as will be seen to be the case in Sect. 3.3), the resultant number of atoms  $N'_i(t)$  of radionuclide  $i$  may be obtained from  $N'_i(t) = \int_{-w}^w N_i(t - \varepsilon) s(\varepsilon) d\varepsilon$ .

For the results in Table 2 in the main body of the text, the parameters fitted were  $r_{11\text{C}}$  or  $r_{13\text{N}}$ ,  $r_{41\text{Ar}}$ ,  $\delta_s$ ,  $\delta_c$ ,  $B_{11\text{C}}$  or  $B_{13\text{N}}$ , and  $B_{41\text{Ar}}$ .

## Appendix 2. Count rates with smearing

In this appendix are developed expressions for fitting to the beam-on-to-beam-off transitions in Sect. 3.5.

Let the transition at time zero between a constant count rate and a decaying count rate be described by:  $c(t) = c_0$ ,  $t < 0$ ;  $c(t) = c_0 \exp(-\lambda t)$ ,  $t \geq 0$ .

Let the count rate  $c(t)$  be smeared by the rectangular function:

$$s(t') = 0, t' < -w; s(t') = 1/(2w), -w \leq t' \leq w; s(t') = 0, t' > w.$$

If the smeared count rate is  $c'(t) = \int_{t-w}^{t+w} c(t') s(t-t') dt'$ , then:

$$c'(t) = c_0, t < -w;$$

$$c'(t) = \{c_0/(2w)\} \{w - t + (1 - \exp(-\lambda(t+w)))/\lambda\}, -w \leq t \leq w;$$

$$c'(t) = \{c_0 \exp(-\lambda t)/(2w\lambda)\} \{\exp(\lambda w) - \exp(-\lambda w)\}, t > w.$$

The integral of the smeared count rate between times  $t_1$  and  $t_2$   $C'(t) = \int_{t_1}^{t_2} c'(t) dt$  is given by summing one or more of the three following integrals with appropriate choices of the limits  $\tau_1$  and  $\tau_2$  ( $\tau_1 \leq \tau_2$ ):

$$I_1(\tau_1, \tau_2) = c_0(\tau_2 - \tau_1), \tau_1 \text{ and } \tau_2 \text{ both } < -w;$$

$$I_2(\tau_1, \tau_2) = \{c_0/(2w)\} \{w(\tau_2 - \tau_1) - (\tau_2^2 - \tau_1^2)/2 + (\tau_2 - \tau_1)/\lambda - (\exp(-\lambda w)/\lambda^2)(\exp(-\lambda\tau_1) - \exp(-\lambda\tau_2))\};$$

$$I_3(\tau_1, \tau_2) = \{c_0/(2w\lambda^2)\} \{\exp(\lambda w) - \exp(-\lambda w)\} \{\exp(-\lambda\tau_1) - \exp(-\lambda\tau_2)\}.$$

For example, if  $t_1 < -w$  and  $t_2 > w$ ,

$$C'(t_1, t_2) = \int_{t_1}^{t_2} c'(t) dt = I_1(t_1, -w) + I_2(-w, w) + I_3(w, t_2).$$

### Appendix 3. Anomalous lines at 835, 847 and 1238 keV

As is shown in Fig. 14, count rates for the three gamma-ray lines at 835, 847 and 1238 keV are anomalous in that they are much higher for the first few months of 2018 than they are thereafter. To investigate the matter further, the 245 gamma-ray spectra accumulated in February 2018 were split into ‘beam on’ and ‘beam off’ categories and summed, and a comparison is shown in Fig. A3.1. It is evident that neither the 847- nor the 1238-keV peak vanish when the synchrotron beam is switched off, and that the 835-keV actually appears to increase when the synchrotron beam is switched off — and so it would seem clear that these lines are not excited by neutron-induced reactions.

The 1238-keV peak might be  $^{214}\text{Bi}$  at 1238.1 keV, but, if so, from the known emission probabilities<sup>16</sup> for  $^{214}\text{Bi}$ , the strength of the peak at 1120 keV ought to be at least twice the strength of the 1238-keV peak — and clearly it is not. The energies of the gamma-ray lines are good to better than  $\pm 0.5$  keV, and from searches on the IAEA NDS database [35] there are no plausible natural radioactivity candidates for the gamma-ray lines at 835 and 847 keV. Consequently, the inevitable suggestion is that the lines at 835, 847 and 1238 keV are due to decay of  $^{54}\text{Mn}$  (834.8 keV) and  $^{56}\text{Co}$  (846.8 and 1238.3 keV) ( $^{56}\text{Co}$  lines at 1038 and 1771 keV are also visible in the spectra).

Fig. A3.2 shows a similar comparison for December 2018. Now none of the peaks at 835, 847 and 1238 keV are present, either with the beam on or with the beam off. The presence of these three ‘anomalous lines’ would therefore appear to have been only temporary.

<sup>16</sup> 14.92% for 1120 keV, 5.83% for 1238 keV [<http://www.nndc.bnl.gov/ndf/b7.1/download.html>].

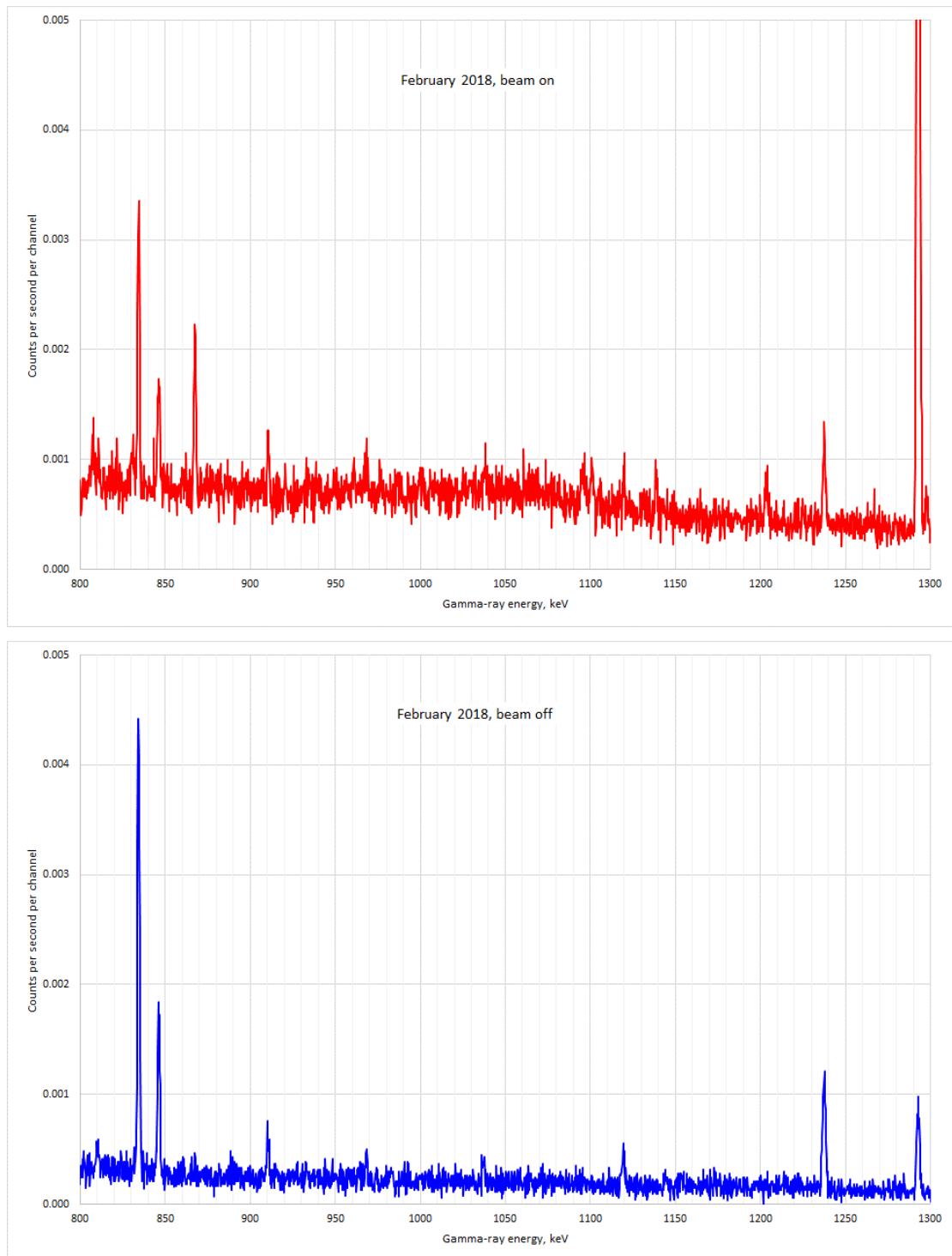


Fig. A3.1. Comparison of ‘beam on’ and ‘beam off’ gamma-ray spectra for February 2018. Beam-on spectra: sum of fifty-nine consecutive 15-minute-long spectra. Beam-off spectra: sum of sixty consecutive 15-minute-long spectra. The 1294-keV peak is  $^{41}\text{Ar}$  (which decays with a half-life of 110 minutes, and so some  $^{41}\text{Ar}$  is still present for a few hours after the beam has been switched off). The peaks at 835, 847 and 1238 keV are present irrespective of whether the beam is on or off.

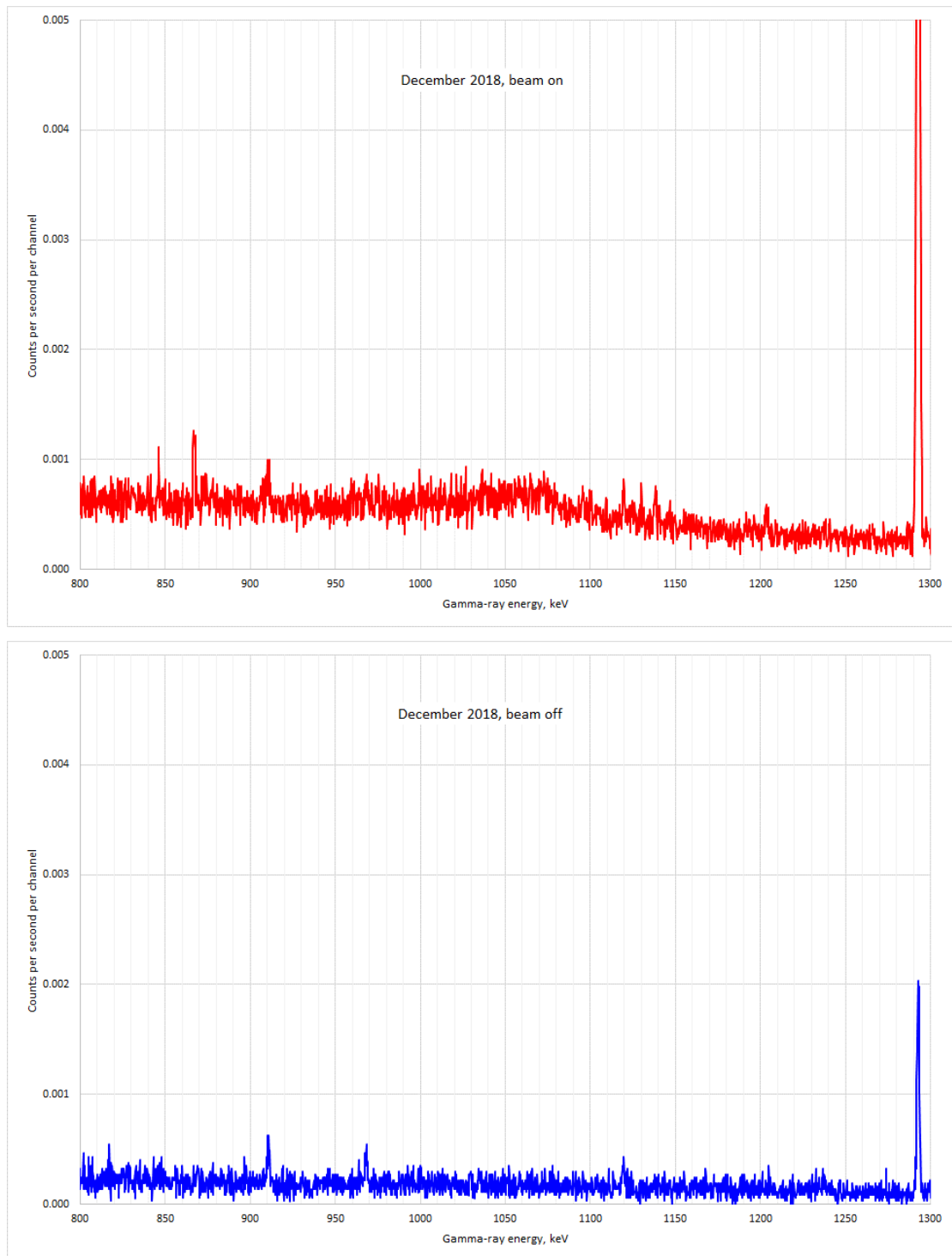


Fig. A3.2. Comparison of ‘beam on’ and ‘beam off’ gamma-ray spectra for December 2018. Beam-on spectra: sum of seventy-five consecutive 15-minute-long spectra. Beam-off spectra: sum of forty-one consecutive 15-minute-long spectra. There are now no apparent peaks at 835, 847 and 1238 keV.

How can the anomalous behaviour of these three gamma-ray lines at 835, 847 and 1238 keV be explained? In principle, at first sight, there are several possible explanations:

- 1) activated material containing  $^{54}\text{Mn}$  and  $^{56}\text{Co}$ , presumably activated steel, incorporated in the support structures for the HPGe gamma-ray detector and its surrounding lead shield;
- 2) activated material containing  $^{54}\text{Mn}$  and  $^{56}\text{Co}$  in the neighbourhood of the HPGe detector but outside its surrounding lead shield;
- 3) airborne dust containing  $^{54}\text{Mn}$  and  $^{56}\text{Co}$  from the inside of the ‘elephant’s trunk’ (the 76-metre-long 10-cm-diameter flexible tube used to suck air out of the synchrotron room and deliver it to the HPGe gamma-ray detector); and
- 4) airborne dust containing  $^{54}\text{Mn}$  and  $^{56}\text{Co}$  in the air in the synchrotron room (especially as the February 2018, March 2018, May 2018, and July 2018 – February 2020 measurements correspond to air taken from four different locations within the synchrotron room, as shown in Table A3.1).

Measurement in	Air sampled from
Feb. 2018	Foil change area
Mar. 2018	SP0 and 9 datum points
May 2018	SP9 datum point and SP6 bridge
Jul. 2018 – Feb. 2020	Hall 2 bridge (inner)

Table A3.1. Regions of the synchrotron room from which air was sampled and measured by the lead-shielded HPGe gamma-ray detector.

Explanation 1 is unlikely, as from Fig. 14 it can be seen that the  $^{54}\text{Mn}$  and  $^{56}\text{Co}$  count rates decay more quickly than the 312-day and 77-day half-lives of  $^{54}\text{Mn}$  and  $^{56}\text{Co}$  respectively.

To distinguish amongst explanations 2–4, the relative strengths of the lines at 847 and 1238 keV can be considered. In the beam-off part of Fig. A3.1, the areas of the 847- and 1238-keV lines are  $0.00942 \pm 0.00056$  and  $0.00933 \pm 0.00050$  counts  $\text{s}^{-1}$  respectively<sup>17</sup> — *i.e.* the strengths of the two peaks are essentially equal. But as listed in Table A3.2, for  $^{56}\text{Co}$  the gamma-ray emission probabilities for the 847- and 1238-keV lines are [22] 99.9% and 66.9% respectively, and for the HPGe gamma-ray detector used for the measurements the full-energy-peak gamma-ray detection efficiency varies<sup>18</sup> as  $E_\gamma^{-1.13}$ . Consequently, the strength of the 1238-keV peak ought to be  $(66.9 \div 99.9) \times (1238 \div 847)^{-1.13} = 0.436$  times the strength of the 847-keV peak — which clearly it is not. However, the energy dependence of the mass attenuation coefficient [36] in lead (Pb) means that a 1238-keV gamma-ray suffers less attenuation

<sup>17</sup> Note that these two count rates are not the same as the corresponding count rates in Table 9, since in Table 9 the count rates are averages over all ten sets of gamma-ray spectra, whereas the count rates given here correspond only to the February 2018 set of gamma-ray spectra.

<sup>18</sup> From  $\epsilon = 1.11\text{E-}02$  and  $3.88\text{E-}03$  at 511 and 1294 keV, and assuming a power law ( $\epsilon \propto E_\gamma^x$ ) where  $E_\gamma$  is the gamma-ray energy. See ISIS-DJSF-20-10-B. The full-energy-peak detection efficiency of *all* HPGe gamma-ray detectors varies as roughly  $1/E_\gamma$ .

in lead than does an 847-keV gamma-ray. The inference is therefore that the source of the  $^{56}\text{Co}$  gamma-rays lies outside the lead shield, and, to achieve the required difference in attenuation, the thickness of lead between the source of  $^{56}\text{Co}$  gamma-rays and the HPGe detector should be<sup>19</sup>  $\sim 3$  cm. This is less than the nominal  $\sim 10$  cm thickness of lead surrounding the air sample vessel and the HPGe gamma-ray detector, but, as is evident in Fig. 4, the shielding is weak at the rear of the detector crystal (essentially zero thickness of lead), and the  $\sim 3$  cm presumably represents some sort of average lead thickness between the source of  $^{56}\text{Co}$  gamma-rays and the HPGe crystal.

Gamma-ray energy, keV	$^{56}\text{Co}$ $\gamma$ emission probability	HPGe f-e-p detection efficiency	Mass atten. coeff. $\mu/\rho$ , Pb, $\text{cm}^2 \text{g}^{-1}$
847	99.9%	0.0063	0.0835
1238	66.9%	0.0041	0.0592

Table A3.2. Quantities involved in detection of gamma-rays from  $^{56}\text{Co}$  ('f-e-p' = full-energy-peak). The detection efficiencies listed are for a distributed gamma-ray source spread uniformly throughout the  $859\text{-cm}^3$  volume of the activated air sample vessel just in front of the HPGe detector.

Consideration of the relative strengths of the 847- and 1238-keV lines has therefore suggested that explanations 3 and 4 are unlikely. Consequently, the most likely explanation would appear to be explanation 2 — *viz* that for the first three measurements in 2018 some activated material was in the neighbourhood of the HPGe detector but outside its surrounding lead shield, but that the activated material was removed before the subsequent measurements were made.

Of course, this deduction about activated material being located outside the lead shield has been able to be made only because  $^{56}\text{Co}$  emits gamma-rays of more than one energy. Since  $^{54}\text{Mn}$  emits gamma-rays of only one energy, it is not possible to deduce its whereabouts by a similar method, but the assumption is being made that the  $^{54}\text{Mn}$  is likely to be associated with the  $^{56}\text{Co}$ .

#### Appendix 4. 'Radon' count rates

If the radon levels in the synchrotron room are similar to the  $\sim 30\text{--}40 \text{ Bq m}^{-3}$  levels measured in the catacombs underneath the synchrotron room (see Sect. 6), radon activity in the  $859\text{-cm}^3$  vessel immediately in front of the HPGe gamma-ray detector sampling air from the synchrotron room could be expected to be  $\sim 0.030 \text{ Bq}$ , and this activity would be the maximum possible activity of the daughter  $^{214}\text{Pb}$  radionuclide. For the  $^{214}\text{Pb}$  352-keV gamma-ray line, the strongest line from  $^{214}\text{Pb}$ , the emission probability is 35.6%, and by scaling by  $1/E_\gamma$  to 352 keV the full-energy-peak detection efficiency of 0.0111 for 511-keV gamma-rays distributed uniformly throughout the air sample vessel (calculated as in Sect. 3.4) to give 0.0161, the maximum possible count rate corresponding to  $\sim 30\text{--}40 \text{ Bq m}^{-3}$  of radon in the air sample vessel would be

<sup>19</sup> If  $\exp(-\mu/\rho_{847} \rho t) = 0.436 \exp(-\mu/\rho_{1238} \rho t)$ , then for  $\rho_{\text{Pb}} = 11.3 \text{ g cm}^{-3}$ ,  $t = 3.02 \text{ cm}$ .

$\sim 0.030 \times 35.6\% \times 0.0161 = \sim 0.00017 \text{ s}^{-1}$ . But, as is evident from Table 9, the actual count rate for the 352-keV line in the background spectrum<sup>20</sup> is  $0.00675 \pm 0.00023 \text{ s}^{-1}$ .

However,  $^{214}\text{Pb}$  is also a decay product of radium ( $^{226}\text{Ra}$ ), and radium (in the  $^{238}\text{U}$  decay chain) is always present in building materials, typical radium concentrations in concrete being of the order of  $\sim 20 \text{ Bq kg}^{-1}$  [37]. A very rough estimate of the likely flux of 352-keV gamma-rays from  $^{214}\text{Pb}$  in equilibrium with  $^{226}\text{Ra}$  in a corridor with concrete floor and walls could be taken as approximately three-quarters<sup>21</sup> of the flux of 352-keV gamma-rays at the centre of a concrete spherical shell<sup>22</sup> containing  $^{214}\text{Pb}$  in equilibrium with  $20 \text{ Bq kg}^{-1}$  of  $^{226}\text{Ra}$  when such a flux  $\phi$  would simply be  $\phi = (3/4) (a\rho/\mu_{352}) \epsilon_{352}$  where  $a$  is the specific activity of  $^{214}\text{Pb}$ ,  $\rho$  is the density of concrete,  $\mu_{352}$  is the linear attenuation coefficient for 352-keV gamma-rays in concrete<sup>23</sup>, and  $\epsilon_{352}$  is the emission probability for the 352-keV line. Putting in the numbers  $a = 0.020 \text{ g}^{-1}$ ,  $\rho = 2.3 \text{ g cm}^{-3}$ ,  $\mu_{352} = \mu/\rho_{352} \rho = 0.231 \text{ cm}^{-1}$ , and  $\epsilon_{352} = 0.356$ ,  $\phi = 0.0532 \text{ cm}^{-2} \text{ s}^{-1}$ .

However, the HPGe detector crystal is shielded by 4 inches of lead, except at the back of the ‘snout’. A rough estimate of the ‘open’ solid angle at the back of the snout is  $\sim 0.50$  steradians<sup>24</sup> (*i.e.* 0.040 of  $4\pi$ ), and an even rougher estimate of the attenuation of gamma-rays in the support structure, cold finger and cryostat at the back of the snout is a factor  $\sim 6$ . Taking the full-energy-peak intrinsic efficiency [38] of 0.320 for 352-keV gamma-rays in a 38-cm<sup>2</sup>-area 2.5-cm-thick planar germanium crystal, the expected count rate would be  $0.0046 \text{ s}^{-1}$ , a count rate not inconsistent with the measured count rate.

---

<sup>20</sup> In the foreground spectrum, there is interference at 352 keV from  $^{56}\text{Fe}(n,\gamma)$ .

<sup>21</sup> The missing one quarter being the roof, assumed not to be concrete.

<sup>22</sup> The particle flux at the centre of a spherical shell source of particles emitted isotropically is simply the number of particles emitted from the shell per unit area and per unit time (assuming no attenuation inside the spherical shell source). The flux at the centre of the spherical shell source from the particles emitted from  $1 \text{ cm}^2$  of surface area of the shell is  $s/(4\pi a^2)$  where  $s$  is the number of particles per second emitted from the shell per square centimetre of surface area and  $a$  (cm) is the radius of the spherical shell, whereupon, by multiplying by the total area  $4\pi a^2$  of the shell, the flux of particles at the centre from the entire surface of the shell is simply  $4\pi a^2(s/(4\pi a^2)) = s$ .

<sup>23</sup> On average, the limiting depth down to which 352-keV gamma-rays can escape from the concrete surface is  $1/\mu_{352}$ .

<sup>24</sup> The centre of the germanium crystal was assumed to be at a depth of 3½ inches inside a 3-inch-diameter hole in the lead shielding.